Journal of Constructional Steel Research 214 (2024) 108440

Contents lists available at ScienceDirect

Journal of Constructional Steel Research

journal homepage: www.elsevier.com/locate/jcsr

Testing, numerical modeling and design of perforated advanced high-strength steel channel section columns

Jia-Hui Zhang [a], Jiaxin Wang [a], Shuluan Xu [a], Fangying Wang [b,*]

[a] Department of Civil Engineering, University of Shanghai for Science and Technology, Shanghai, China
[b] Department of Civil Engineering, University of Nottingham, Nottingham, UK

ARTICLE INFO

Keywords:
Axial compression
Axial stiffness
Buckling instability
High-strength steel
Perforated C-section

ABSTRACT

This paper examines the influence of perforations on the buckling instability and load-bearing capacity of advanced high-strength steel channel section (C-section) columns. Experimental tests were first conducted on 19 column specimens made of complex phrase steel HC700CP980 under axial compression, followed by finite element (FE) analysis. Two section types, the flat web C-section and the web-stiffened C-section, were considered, with perforations categorised as web-only or both web and flanges. Material tests and initial imperfection measurements were conducted and reported. Using test results, finite element models were established and parameter analysis was carried out. Analysis of test results and finite element data revealed that perforations had a noticeable impact on the buckling deformation of flat web C-sections but had a minor effect on load-bearing capacity. In contrast, web-stiffened C-sections exhibited intensified deformation post-perforation, significantly reducing their axial stiffness and load-bearing capacity. The Direct Strength Method (DSM) was assessed based on combined test and FE data. It revealed that the DSM resulted in a high level of inaccuracy and scatter in the load-bearing capacity predictions of high-strength steel C-sections after perforation. To address this, a modified method incorporating a perforation strength reduction factor was proposed, offering straightforward and intuitive calculations with improved design accuracy and consistency.

1. Introduction

Cold-formed thin-walled steel members are a prominent choice within the realm of engineering due to their attributes, including their lightweight construction, high strength, and versatility in cross-sectional configurations. Perforations are strategic openings made within these steel sections to facilitate the passage of utilities and provide structural adaptability. While this practice offers practical benefits, it necessitates a comprehensive understanding of its consequences on the structural behavior of these members. Notably, the perforation may lead to changes in the stress distribution, buckling deformation, and load-bearing capacity of the structural members.

A considerable number of studies have focused on thin-walled perforated components made of medium and low strength steels. Moen and Schafer [1–3], Smith and Moen [4] systematically studied cold-formed steel columns with holes through a series of experimental, numerical and theoretical investigations, and proposed reduction calculation methods for global, local, and distortional buckling critical loads for perforated C-sections. These reduction calculation methods have subsequently been adopted by AISI 2016 [5] for cold-formed steel perforated members. Kulatunga et al. [6,7] found that the ultimate strength of C-section columns is significantly affected by variations in the form and placement of perforations. Zhao et al. [8–10] investigated the effects of perforation width, eccentric loading, and simple supports on the structural behavior of perforated specimens; a simplified calculation method was also proposed. Moreover, Chen et al. [11,12] observed that the edge-stiffened hole-section members were capable of achieving higher load-bearing capacities than their plain section counterparts.

Web-stiffened open-section columns are extensively employed in structural applications, primarily owing to their improved local stability. However, limited research has focused on the behavior of such sections with perforation. Yao and Rasmussen [13,14] performed finite element parametric analyses and indicated the necessity to account for the interaction between distortional and global buckling phenomena in load-bearing calculations for web-stiffened C-sections, irrespective of the presence of perforations. Zhang and Alam [15,16] proposed an elastic buckling stress extraction method for stiffened Rack sections, and

* Corresponding author.
E-mail address: Fangying.wang@nottingham.ac.uk (F. Wang).

https://doi.org/10.1016/j.jcsr.2023.108440
Received 24 October 2023; Received in revised form 12 December 2023; Accepted 26 December 2023
Available online 5 January 2024

noted inaccuracy and potential safety concerns associated with the application of the direct strength method in load-bearing calculations for such sections.

Advanced High Strength Steel (AHSS) exhibits a more intricate microstructure in comparison to conventional high-strength steel (HSS). This complex microstructure is attained through a precisely controlled smelting process that renders AHSS with superior strength and remarkable ductility. The AHSS can be generally catogorised in to dual-phase steel (DP), complex-phase steel (CP), martensitic steel (MS), and twinning-induced plasticity steel (TWIP). Given its widespread application in the automotive industry and advancements in manufacturing techniques, the production costs of DP and CP steels are gradually converging with those of conventional HSS, highlighting their substantial potential in applications involving light gauge steel structures. Nevertheless, the research exploring their use in thin-walled components remains scarce. The only existing documented research available, as reported in Yan et al. [17–19], investigated the material properties of these steels. In practical applications, C-sections typically feature plate thicknesses ranging from 1.0 to 1.6 mm for light-gauge structures, with the prevalent use of S355. In Australia, there is a precedent for employing S550 steel in housing construction by reducing the thickness to 0.7 mm [20]. This application has demonstrated the potential of advanced high-strength steel in further reducing the weight of wall panels. The application of advanced high-strength steel extends to various structural components, including stocky columns, bottom chords in trusses, and tension bars in bridges, particularly for members featuring perforations.

This paper focuses on the axial compression performance of perforated CP steel thin-walled members. Two types of open sections were investigated: flat-webbed C-sections and web-stiffened C-sections, with perforation positions including web perforation only and both web and flange perforation. The influence of perforation number and position on the buckling deformation and ultimate load-bearing capacity of C-sections was first examined through experiments and finite element analyses. Subsequently, the appropriateness of the current direct strength method to the studied CP steel thin-walled perforated axial compression columns was evaluated. Finally, a modified design method using strength reduction coefficient, suitable for CP steel perforated C-section columns, was proposed.

2. Axial compression tests

2.1. Specimen cross-section design, labeling, and preparation

In this study, the cold-formed thin-walled steel compression members were fabricated using high-strength complex-phase steel (HC700CP980) plates, and the chemical composition of this material is shown in Table 1. The nominal yield stress and ultimate tensile strength of HC700CP980, were 700 MPa and 980 MPa, respectively. The steel plate had a nominal thickness of 1.0 mm. The cross-sectional profiles of the thin-walled members are shown in Fig. 1, where C1 denotes a simple lipped channel section, and C2 denotes a simple lipped channel section with a web stiffener. The nominal dimensions for the C1 and C2 sections are as follows: the overall height of the web (W) was 100 mm, the flange width (F_1 and F_2) was 40 mm, the lip length (l_1 and l_2) was 15 mm, and the stiffener dimension (W_2 and W_3) was 21 mm. The axial compressive test specimens have slotted holes that include holes in the web only and holes in both the web and flange. These holes were centrally arranged in terms of web height and flange width. Three different member lengths were examined in the column tests, including 300, 900, and 1500 mm. A total of 19 column specimens were examined in the experimental study, of which 14 were C1-section and 5 were C2-section. Detailed measured geometric dimensions of the C1 and C2 specimens are shown in Tables 2 and 3, respectively.

Table 1
Chemical composition of high-strength complex-phase steel.

Grade	C%	Si%	Mn%	P%	S%	Al total %
HC700CP980	0.162	0.332	1.65	0.008	0.001	0.037

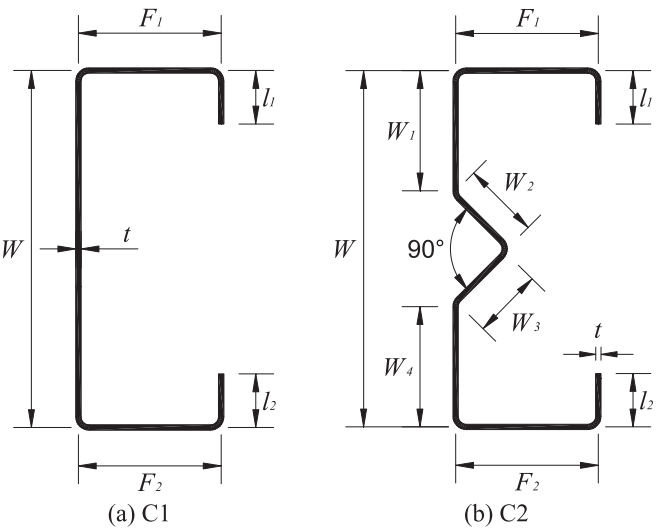

Fig. 1. Definition of symbols for C-sections.

The labeling for the specimens comprises information related to the cross-sectional profile, axial length of the member, slotted hole position, and the number of slotted holes, as described in Fig. 2. For example, C1L900-F1W1 denotes a specimen from C1 series (a simple lipped channel section) with a nominal member length of 900 mm and one slotted hole in both the flange and web. A letter "R" is used for the repeat specimen. The geometric dimensions of the slotted holes in the web and flange and their relative locations along the column length are illustrated in Fig. 3. The width of the slotted holes (W_H) was taken equal to 0.4 times the height of the web or the width of the flange according to their respective locations, and the length of the slot (L_H) was set as 100 mm and 55 mm respectively for holes in the web and flange, respectively. It is worth noting that, for specimens with holes in both the web and flange (i.e. for C1L300-F1W1, C1L900-F1W1, C1L1500-F1W1 and C1L1500-F2W2), the centres of the holes were assigned at the same cross-sections along the specimen.

Special care was taken during the fabrication of the channel section specimens. Firstly, the high strength steel plates were cut using a fiber laser machine and holes were laser-drilled at specific positions based on the geometric dimensions of the cross-sectional design. Subsequently, the machined plate underwent multiple stamping and bending operations to conform to the cross-sectional profiles outlined in Fig. 1. Lastly, the ends of the specimens were affixed to U-shaped tracks using bolts. This is to simulate the constraint boundary condition between the vertical C-shaped studs and horizontal U-shaped runners commonly used in a light steel stud wall. Prior to attaching the specimen to U-shaped tracks, the ends of the specimens were ground smooth to ensure full contact with the web face of the tracks.

2.2. Material properties

The mechanical properties of the high-strength complex-phase steel were examined through longitudinal coupon tests. Three coupon specimens were taken from the same batch of the steel plates used for the column specimens. The tensile testing was performed using a Zwick Z100 universal material testing machine, and the testing procedure and loading rate conformed to the standard for tensile testing of metallic materials in the Chinese Standard GB/T 228.1–2021 [21]. A contact extensometer, with a gauge length of 25 mm and a sampling frequency of 10 Hz, was used to measure the elongation of the specimen. The

Table 2
Measured dimensions of C1-section specimens.

Specimen ID	L/mm	t/mm	W/mm	F_1/mm	F_2/mm	l_1/mm	l_2/mm
C1L300	300	1.004	99.83	39.94	39.70	14.76	14.81
C1L300R	300	1.007	99.80	39.53	39.79	14.76	14.52
C1L300-W1	300	1.008	99.81	40.30	39.98	14.48	14.90
C1L300-W1R	300	1.004	99.89	39.79	39.60	14.72	14.75
C1L300-F1W1	300	0.998	101.81	39.66	40.39	14.78	15.27
C1L900	900	0.997	99.91	40.01	39.50	14.62	14.85
C1L900R	900	0.994	100.42	39.71	39.60	14.68	14.88
C1L900-W1	900	1.000	100.45	39.77	39.98	15.17	14.66
C1L900-F1W1	900	1.000	100.34	39.31	39.79	14.81	14.84
C1L1500	1500	1.006	99.85	39.88	39.63	14.78	14.68
C1L1500-W1	1500	1.001	100.15	39.76	39.64	14.77	14.74
C1L1500-W2	1500	0.997	99.95	39.60	39.81	14.89	14.47
C1L1500-F1W1	1500	0.997	100.10	39.50	39.44	15.10	14.72
C1L1500-F2W2	1500	0.996	100.10	39.17	39.63	14.88	14.78

Table 3
Measured dimensions of C2-section specimens.

Specimen ID	L/mm	t/mm	W/mm	W_1/mm	W_2/mm	W_{13}/mm	W_4/mm	F_1/mm	F_2/mm	l_1/mm	l_2/mm
C2L900	900	1.006	101.75	36.11	21.04	20.82	35.96	39.29	39.49	13.79	14.17
C2L900-W1	900	1.008	101.13	35.29	20.92	21.09	35.37	39.18	39.41	13.36	13.84
C2L1500	1500	0.997	100.72	35.52	20.12	20.76	35.91	39.84	39.46	14.79	15.16
C2L1500-W1	1500	1.008	101.36	35.85	20.81	20.40	36.86	39.30	38.99	13.96	14.24
C2L1500-W2	1500	0.987	101.22	36.27	20.60	20.75	36.36	39.08	39.44	13.95	13.82

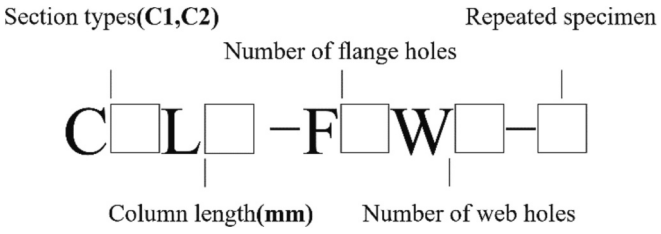

Fig. 2. Specimen labelling system.

typical stress-strain curve for the high-strength complex-phase steel is shown in Fig. 4. The complex-phase steel exhibits no noticeable yield plateau, thus the 0.2% proof stress was used to represent the yield stress. Table 4 summarises the material properties obtained from the tests, where E represents the elastic modulus, $\sigma_{0.2}$ and σ_u correspond to the yield stress and ultimate tensile strength, and ε_f represents the strain at fracture.

2.3. Measurement of initial geometric imperfections

The structural behavior and axial compressive resistances of thin-walled steel members are known to be influenced by their initial geometric imperfections [22–24]. Therefore, the initial global and local geometric imperfections were measured prior to column testing. These measurements were executed using a three-coordinate measuring machine with a precision of 0.001 mm. Before the formal measurement, the probe of the machine was calibrated to determine the reference points for measurement, ensuring test accuracy, as depicted in Fig. 5(a).

The initial geometric imperfections of thin-walled components can generally be classified as local deformations, distortion deformations,

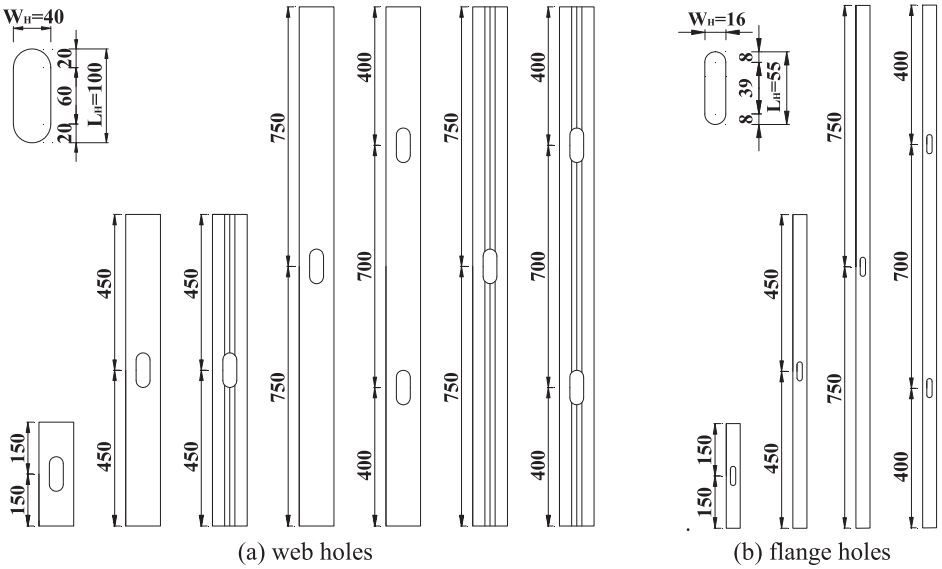

Fig. 3. Locations and dimensions (in mm) of web and flange holes.

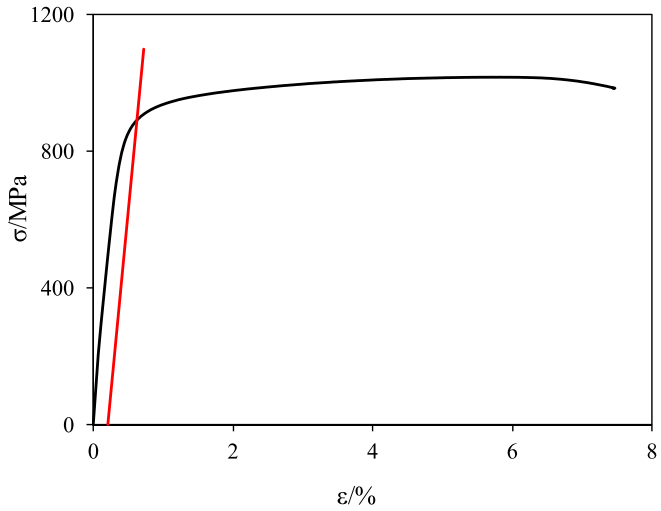

Fig. 4. Stress-strain curve of CP980.

Table 4
Measured material properties of high-strength complex-phase steel.

Coupon Specimen	E/GPa	$\sigma_{0.2}$/MPa	σ_u/MPa	ε_f/%
Coupon-1	213.9	889.7	1017.5	7.47
Coupon-2	215.3	866.9	1028.4	8.20
Coupon-3	221.0	882.4	1014.0	6.63

and overall deformations. The layouts of measurement points for C1 and C2 sections are presented in Figs. 5(b) and 5(c), where the vertical axis refers to the reading for initial imperfection and the horizontal axial refers to the normalized coordinate. The W1, W2, W3, and W4 points were used to measure the overall and local initial geometric imperfections along the axial direction of the web. F1 and F2 points were designated for the measurement of distortion imperfections along the axial direction of the flange. Note that the measured geometric imperfection amplitudes are taken as positive if the negative data recorded by the respective LVDT (shortening of the probe in the LVDT). The interval distance of measurement points along the member length varied from 3 to 5 cm.

Considering data coordinates measured along the length from the start to end as a linear reference, the presence of intermediate measurement data lies above this reference indicates an outward deformation (i.e. the overall profile bowing towards the web); otherwise, it denotes a concave deformation. This approach allows for the determination of both the overall and distortion initial geometric imperfections. Two examples of the measured geometric imperfections are depicted in Fig. 6, with the statistic results summarised in Table 5. It can be seen that the most significant distortion imperfections manifest as outward deformation, with peak values of 0.825 mm and 0.833 mm. The largest overall imperfections also present as outward deformation, with peak values of 0.899 mm and 0.972 mm. For initial local geometric imperfection measurement, using the straight line connecting measurement points on both sides of the web (W1 and W3 for C1-section, and W1 and W4 for C2-section, as shown in Fig. 5) as a reference, the local initial geometric imperfections at the corresponding locations on W2 (for C1-section) or both W2 and W3 (for C2-section) can be determined. For both section types, the most significant local imperfections show inward deformations with peak values of −0.512 mm and − 1.484 mm.

2.4. Column test setup

The axial compressive column tests on the thin-walled high strength steel channel section specimens were carried out using the 500 kN capacity POPWARE self-balancing frame-type electro-hydraulic structural testing system. A diagram of the column test setup is shown in Fig. 7. Prior to testing, the U-shaped runners were first secured at both ends of the specimen using bolts, and then the specimen was placed onto a rigid support plate. The relative positions of the specimen, runners, and loading head were precisely aligned using the laser level in the direction of axial loading. Upon alignment, C-clamps were used to fix the upper and lower U-shaped runners to the upper rigid end plates and lower rigid support, respectively.

The instrumentations employed for the C1-section and C2-section columns are shown in Fig. 8 (a) and (b), respectively. A total of three axial displacement transducers and four lateral displacement transducers were placed for C1-section columns, while two additional lateral displacement transducers were used for C2-section columns in order to detect lateral deformations at the web stiffener. The layout of the displacement transducers is presented in Fig. 8. The axial displacement transducers were arranged in a triangular layout to obtain the load-axial displacement curves. The lateral displacement transducers were placed

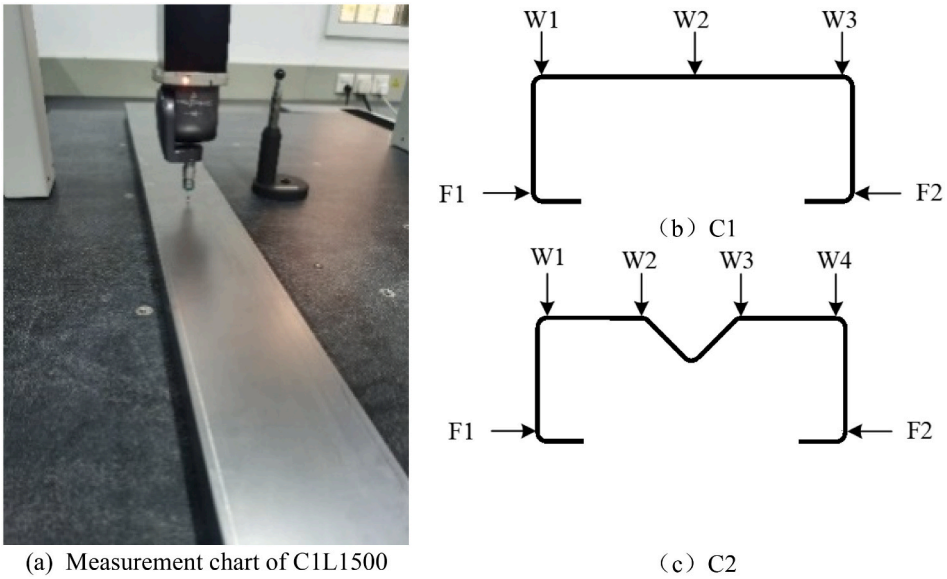

Fig. 5. Measurement of the initial geometric imperfections.

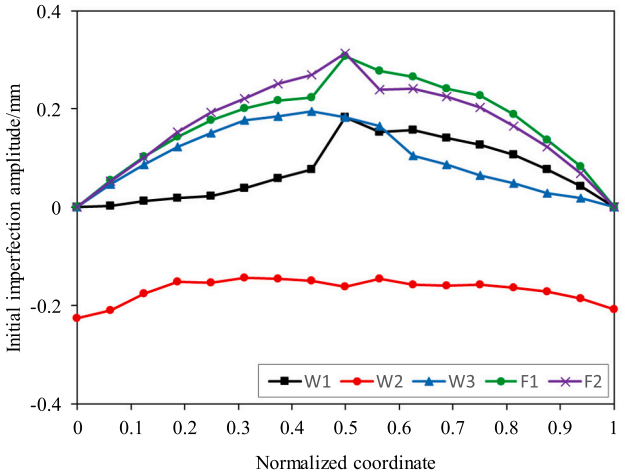

(a) Initial geometric imperfections of C1L900R

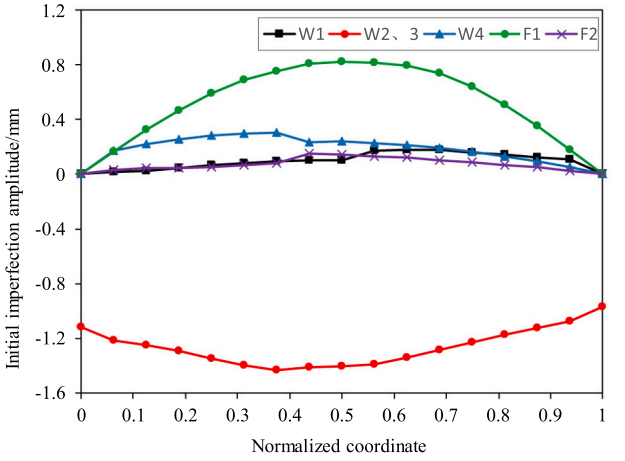

(b) Initial geometric imperfections of C2L900

Fig. 6. Initial geometric imperfections of specimens.

Table 5
Measured initial local, distortional and overall geometric imperfections.

Specimen ID	Local/mm	Distortional/mm	Overall/mm
C1L300	− 0.255	0.069	0.055
C1L300R	− 0.271	0.122	0.128
C1L300-W1	− 0.196	0.107	0.129
C1L300-W1R	− 0.098	0.065	0.046
C1L300-F1W1	− 0.129	0.117	0.310
C1L900	− 0.318	0.541	0.433
C1L900R	− 0.226	0.314	0.194
C1L900-W1	− 0.341	0.162	0.227
C1L900-F1W1	− 0.187	0.397	0.349
C2L900	− 1.433	0.825	0.301
C2L900-W1	− 0.732	0.627	0.264
C1L1500	− 0.214	0.494	0.115
C1L1500-W1	− 0.304	0.538	0.120
C1L1500-W2	− 0.512	0.803	0.199
C1L1500-F1W1	− 0.467	0.715	0.389
C1L1500-F2W2	− 0.446	0.378	0.899
C2L1500	− 1.403	0.479	0.218
C2L1500-W1	− 1.484	0.790	0.217
C2L1500-W2	− 0.875	0.833	0.972

at the midpoint of the component, facilitating measurements of the overall buckling and distortion buckling of the component.

Special care was taken during the load application to the specimens. To ensure evenly distributed axial loading, a preload equal to 25% of the estimated ultimate strength was applied. Deviations of no more than ±10% in readings from the three axial displacement transducers during the preload can confirm the uniform axial load applications. The axial loads were applied at a constant loading rate of 0.25 mm/min and terminated when the load dropped to approximately 80% of its peak value. Throughout the test, a data acquisition device was used to record readings from the displacement transducers and the loading.

3. Experimental results

The ultimate strengths of the examined CP steel thin-walled C-section members under axial compression and their failure modes are summarised in Tables 6 and 7. The symbols are used to denote buckling modes: “L” for local buckling, “D” for distortional buckling, “F” for flexural buckling, “T” for torsional buckling, and “+” to signify the interaction between buckling modes. Meanwhile, the losses of load-bearing capacity of components with slotted holes compared to their counterparts without holes are reported.

3.1. Failure mode and load-bearing capacity of C1-section

It was observed that the C1-section specimens exhibited buckling interactions. The stub column of section C1 (L = 300 mm) showed interactions between local buckling and distortional buckling. The medium-short column of C1-section (L = 900 mm) presented local and distortional buckling interactions, with some specimens exhibiting torsional buckling. The medium-long columns of section C1 (L = 1500 mm) exhibited interactions among local buckling, distortional buckling, and flexural buckling, with some accompanied by torsional buckling.

The presence of holes in the web had a notable impact on the load-bearing capacity and buckling behavior of the components. The instability failure mode of the C1-section stub columns, with a nominal length of 300 mm, is illustrated in Fig. 9. Unperforated members (C1L300) displayed interaction of local and distortional buckling. In the specimen with a single web hole (C1L300-W1), instability primarily occurred around the holes, with noticeable deformation on the flanges at the same height adjacent to the holes, leading to a load-bearing capacity reduction of approximately 10%. For the specimen with perforated holes in both the web and flange (C1L300-F1W1), significant deformations were evident at both hole locations, extending into the adjacent corner regions. Consequently, the reduction in load-bearing capacity for this specimen exceeded 20%.

The presence of web perforations exacerbated distortional buckling deformations in C1-section specimens as the length of the specimens increased. As shown in Fig. 10, unperforated members (C1L900) experienced interactions of local, distortional, and torsional buckling. Specimens with web holes (C1L900-W1) displayed an inward deformation of the flange, indicating an I-shaped distortional buckling. The specimen C1L900-F1W1, featuring perforations in both the web and flange, exhibited more pronounced distortional buckling with compromised flange stability and resulted in a 19.2% reduction in load-bearing capacity.

The influence of the numbers of web perforations were studied in the series of medium-long columns (L = 1500 mm). As illustrated in Fig. 11, the unperforated specimen (C1L1500) exhibited more continuous local buckling deformations on the web compared to perforated counterparts, with negligible distortional buckling deformations. Specimen with a single web hole (C1L1500-W1) displayed interrupted local buckling deformations around the hole, but distortional buckling deformations were evident at the height of the hole on the flange. For specimen with holes at both the web and flange (C1L1500-F1W1), it appeared that axial stiffness was further compromised at the perforation height, resulting in symmetric local and distortional buckling deformations along the axial direction of the perforation. The most significant distortional buckling, characterized as I-shaped, occurred at the location of the perforation. Compared to specimens with a single hole, those with two holes showed

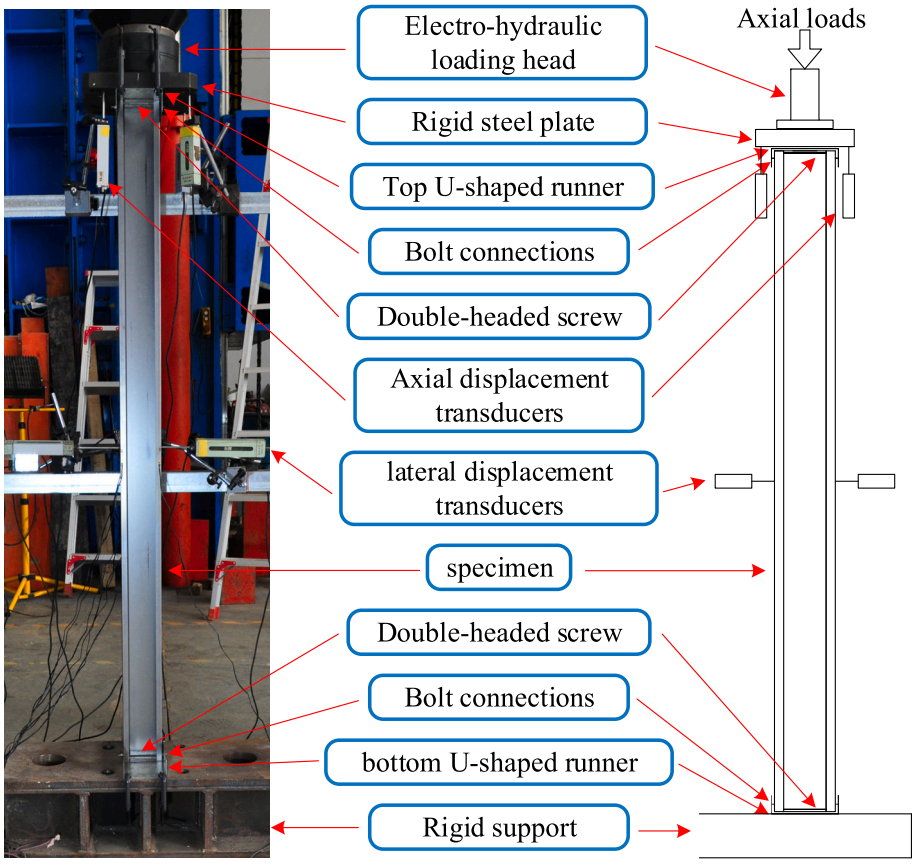

Fig. 7. Test setup.

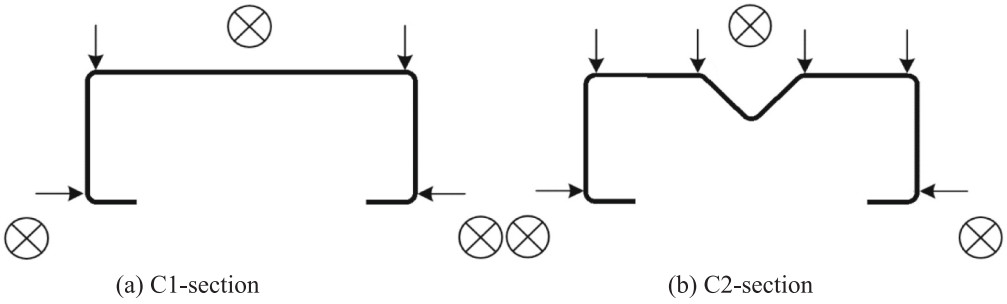

Fig. 8. Locations of axial and lateral displacement transducers.

Table 6
Test compression capacities and failure modes of C1-section column specimens.

Specimen ID	P_{Test}/kN	Failure mode	Loss of load-bearing capacity/%
C1L300	82.20	L + D	/
C1L300R	80.52	L + D	/
C1L300-W1	74.24	L + D	9.7
C1L300-W1R	72.38	L + D	11.9
C1L300-F1W1	62.41	L + D	24.1
C1L900	60.63	L + D + FT	/
C1L900R	61.88	L + D	/
C1L900-W1	55.32	L + D + F	8.8
C1L900-F1W1	48.96	L + D + F	19.2
C1L1500	52.84	L + D + FT	/
C1L1500-W1	49.12	L + D + FT	7.0
C1L1500-W2	47.11	L + D + FT	10.8
C1L1500-F1W1	45.73	L + D + F	13.5
C1L1500-F2W2	41.92	L + D + F	20.7

Table 7
Test compression capacities and failure modes of C2-section column specimens.

Specimen ID	P_{Test}/kN	Failure mode	Loss of load-bearing capacity/%
C2L900	76.38	D + F	/
C2L900-W1	61.35	D + F	19.7
C2L1500	60.58	D + FT	/
C2L1500-W1	54.88	D + FT	9.4
C2L1500-W2	44.54	D + FT	26.5

a more pronounced decrease in load-bearing capacity.

3.2. Failure mode and load-bearing capacity of C2-section

For C2-section specimens, the introduction of web stiffener significantly enhanced the local buckling stability. This led to a transition in the failure mode of C2-section members from local buckling to the interaction of distortional buckling and overall instability. Generally,

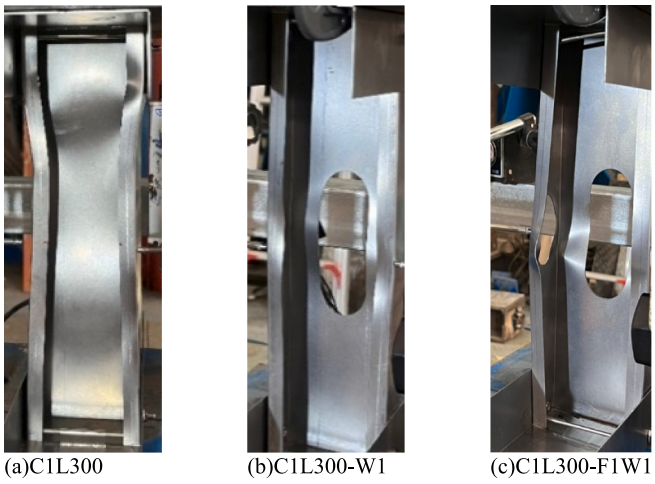

Fig. 9. Failure modes of C1-section specimens with a length of 300 mm.

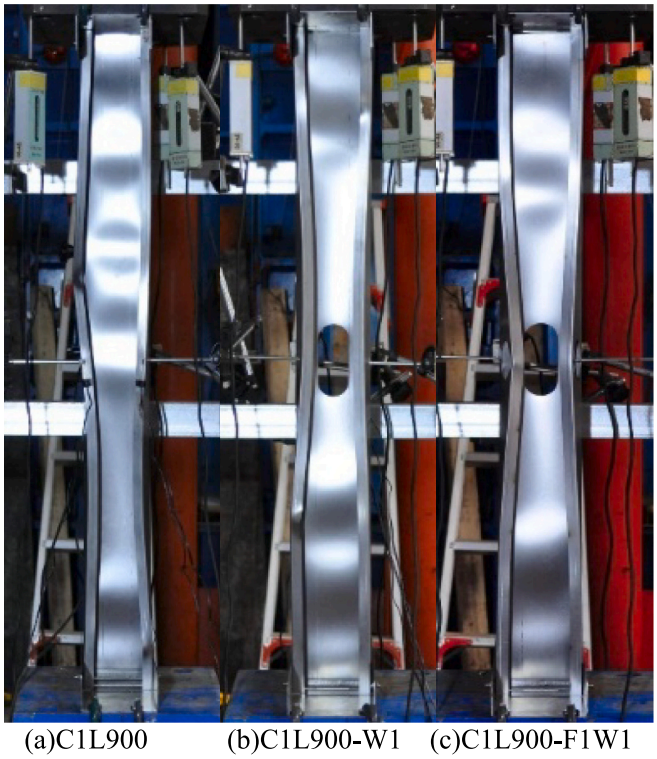

Fig. 10. Failure modes of C1-section specimens with a length of 900 mm.

C2-section exhibited a substantial enhancement in the ultimate capacity when compared to the C1-section. Table 7 summarises the ultimate load-bearing capacity, failure modes, and load-bearing capacity reduction of all the C2-section specimens. Distinct flange distortional buckling deformations were evidently shown in the medium-short C2-section columns (L = 900 mm), as depicted in Fig. 12. The specimen with a single web hole (C2L900-W1) displayed more pronounced distortional buckling deformations, primarily concentrated at the hole location. Compared to the unperforated specimen, a high level of capacity reduction equal to 19.7% was found in specimen C2L900-W1. This indicates that, though the introduction of web stiffeners enhanced the ultimate capacity, as seen by the comparisons of C2L900 and C1L900, the strength enhancement has been significantly compromised by the hole in the web.

For the medium-long C2-section columns (L = 1500 mm),

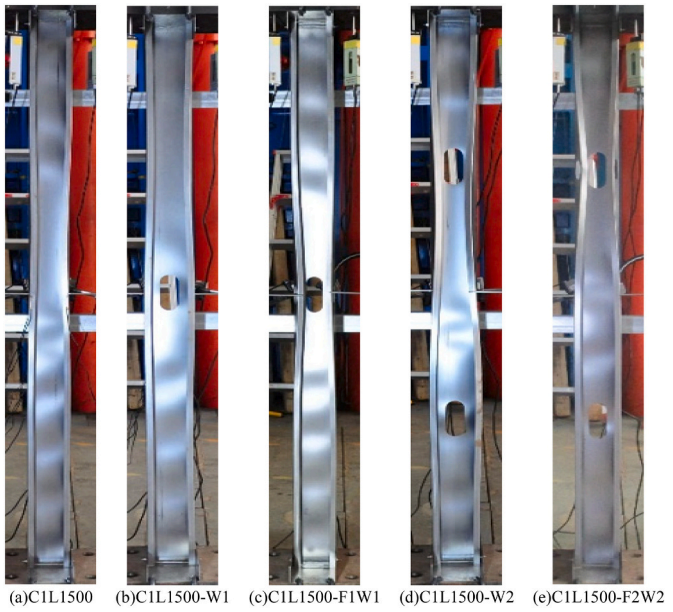

Fig. 11. Failure modes of C1-section specimens with a length of 1500 mm.

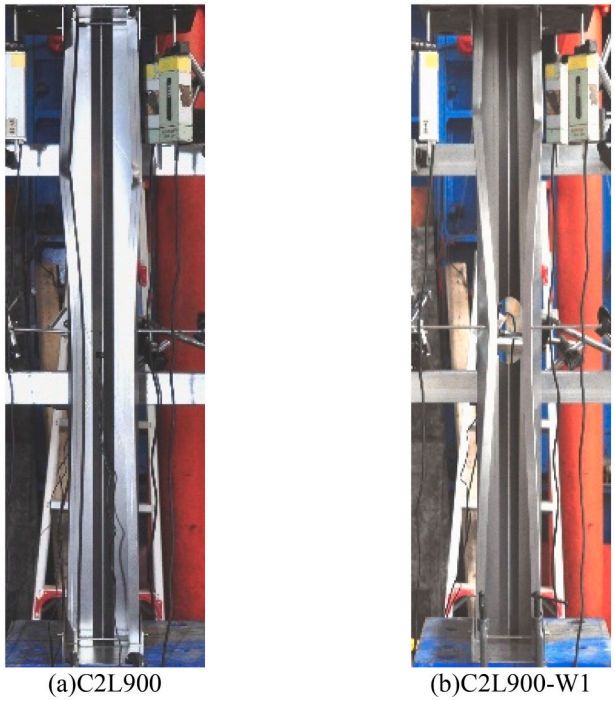

Fig. 12. Failure modes for C2-section specimens with a length of 900 mm.

distortional buckling deformations of the flange were observed, especially around the hole areas in the flange, as shown in Fig. 13. The specimen with two holes (C2L1500-W2), compared to that with a single hole (C2L1500-W1), experienced a more pronounced reduction in load-bearing capacity, with the capacity loss increasing from 9.4% to 26.5%. Additionally, in comparison to C1-section specimens, the loss in load-bearing capacity for C2-section specimens with a single hole increased from 7.0% to 9.4%, and for those with two holes, it rose from 10.8% to 26.5%. Overall, the axial compression test results for C1-section and C2-section specimens reveal the following key findings:

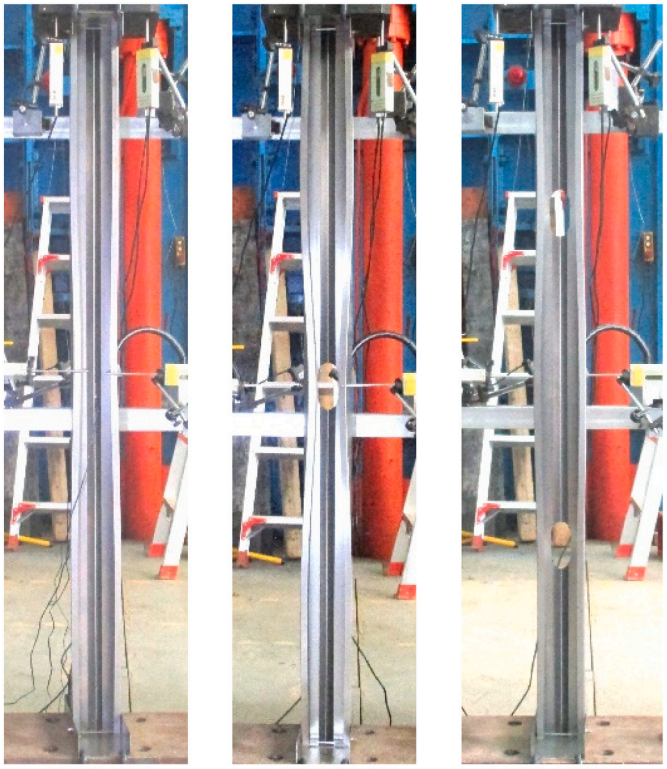

(a)C2L1500 (b)C2L1500-W1 (c)C2L1500-W2

Fig. 13. Failure modes for C2-section specimens with a length of 1500 mm.

1. The larger width-to-thickness ratio of the web in C1-section specimens primarily led to local buckling deformations. The presence of holes in the web reduced the load-bearing capacity of C1-section specimens, with an increase in the reduction of load-bearing capacity as the number of holes increased.
2. The presence of web stiffener in the C2-section specimens improved the local buckling stability of the specimens, changing the failure mode to flange distortional buckling. In comparison to perforated C1-section specimens, the perforated C2-section specimens exhibited a higher reduction in load-bearing capacity.
3. The reduction in load-bearing capacity in C1-section specimens may be attributed to the disruption in the continuity of local buckling deformations caused by the holes, leading to a decrease in the post-buckling capacity of the specimens. In contrast, the primary reason for the reduction in load-bearing capacity in C2-section specimen is mainly the decrease in axial stiffness due to holes in the stiffened web areas.

4. Finite element modeling and parametric study

Finite element analyses were conducted to assess the impact of perforations on the axial compression stability of the examined CP steel thin-walled channel section columns. Upon validation of finite element models, a systematic parametric study was undertaken to determine the correlation between the number of perforations and the load-bearing capacity of these structural members. The numerical results have mirrored the test observations, showing a reduction in load-bearing capacity for C1- and C2-section specimens when web perforations were present, with a further loss observed when both the web and flange were perforated.

4.1. Finite element modeling and verification

In this section, the general finite element software ABAQUS was used to model CP-steel thin-walled channel specimens. The model utilised S4R shell elements due to their effectiveness in representing buckling instability. The geometric dimensions of the finite element model adopted the measured dimensions of the test specimens. Material properties in the model were derived after converting the engineering stress-strain curve, measured by tensile coupon tests herein, to the true stress-strain curve. The mesh was refined around section corners and holes with a mesh size of 5 mm × 5 mm. To introduce initial imperfections, modal coordinates for local buckling, distortional buckling, and flexural buckling were obtained through an elastic eigenvalue buckling analysis. These coordinates were combined with measured initial imperfection values and imported into the model.

The boundary conditions were achieved by coupling the end faces of the specimen to the reference points (RP) with appropriate degree of freedom settings, as shown in Fig. 14. In the experiments, the specimens were affixed to a U-shaped guide runner. To account for the variable constraint strength, ranging between fixed-fixed and pinned-pinned supports, an attempt was made to increase the constraint at the reference point gradually. The modeling was based on three boundary conditions: pinned-pinned (K = 1), pinned-fixed (K = 0.7), and fixed-fixed (K = 0.5). In this context, K is denoted as the effective length factor. The load-bearing simulation values for these three examined conditions are presented in Table 8. It can be found that the values corresponding to an effective length factor of K = 0.7 are in best agreement with the experimental results, exhibiting the smallest deviation. The typical load versus axial shortening curves for the column specimens, as predicted by FE analysis and obtained in tests, are presented in Fig. 15 (a) and (b) for specimens C1L1500-W1 and C1L900, respectively, demonstrating good agreements. Additionally, the deformation patterns at ultimate loads in the finite element models of C1- and C2-section specimens were compared with those of the experimental specimens, as depicted in Fig. 16. The finite element models effectively replicated the buckling deformations in both perforated and unperforated specimens. Therefore, an effective length factor of K = 0.7 was adopted for subsequent finite element analysis.

4.2. Parametric study

Upon validating the experimental data with the finite element models, a parametric study was initiated to explore the effects of holes on the stability of the examined thin-walled channel section specimens. The number of holes was determined based on the axial length of the specimens considering their practical uses. Specifically, for C1-section stub columns (L = 300 mm), one hole was located in the web. In the case of C1-section medium-short columns (L = 900 mm), the number of web holes was increased to three. For C1-section medium-long columns (L = 1500 mm) and long columns (L = 2000 mm), a maximum of five web holes were incorporated. The equivalent C2-section specimens featured an identical number of holes as their C1-section counterparts. In the specimen FE models of both the C1- and C2-section with axial lengths of 300 and 900 mm, one hole was designed for both the web and the flange. For specimen FE models with axial lengths of 1500 and 2000 mm, one or two holes were considered in both the web and the flange. Plate thicknesses of 0.6 mm, 1.0 mm, and 2.0 mm were employed for the specimens herein. In total, 132 specimens were generated with parameter details summarised in Table 9.

Additionally, to assess the variation in load-bearing capacity of specimens with holes under different strength grades of steel, high-strength steel (G500) and carbon structural steel (Q235) were incorporated into the parametric analysis for comparison with the advanced high-strength steel (CP980). For the finite element models with the plate thickness of 1.0 mm, the material properties of G500 (with nominal yield strength and actual yield strength of 500 MPa and 604 MPa, respectively) and Q235 (with nominal yield strength and actual yield strength of 235 MPa and 313 MPa, respectively) were imported. In the strength comparison, there were 44 finite element specimens each for

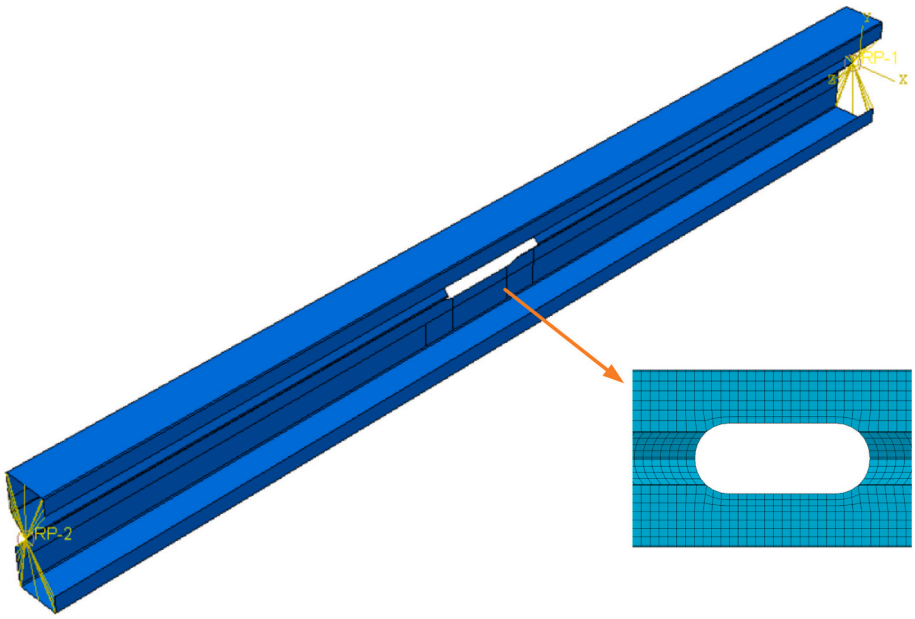

Fig. 14. Finite element model for C2L900-W1.

Table 8
Comparison of test and FE results.

Specimen ID	P_{Test}/P_{FEA} (K = 0.5)	P_{Test}/P_{FEA} (K = 0.7)	P_{Test}/P_{FEA} (K = 1.0)
C1L300	0.95	0.99	1.04
C1L300R	0.93	0.97	1.02
C1L300-W1	0.96	0.96	1.11
C1L300-W1R	0.93	0.93	1.08
C1L300-F1W1	0.88	0.98	1.14
C1L900	0.80	0.97	1.27
C1L900R	0.81	0.99	1.29
C1L900-W1	0.79	0.92	1.28
C1L900-F1W1	0.76	0.90	1.29
C2L900	0.87	0.96	1.18
C2L900-W1	0.90	0.94	1.28
C1L1500	0.74	1.04	1.81
C1L1500-W1	0.76	1.00	1.73
C1L1500-W2	0.70	0.97	1.64
C1L1500-F1W1	0.74	0.96	1.63
C1L1500-F2W2	0.65	0.92	1.49
C2L1500	0.72	0.92	1.55
C2L1500-W1	0.91	1.09	1.85
C2L1500-W2	0.71	0.95	1.61
Pm	0.81	0.97	1.38
COV	0.120	0.049	0.195

G500 and Q235, making a total of 88 specimens.

4.3. Discussion of parametric study for perforated columns

The influence of holes on the buckling failure mode and load-bearing capacity of the thin-walled channel section perforated columns is investigated by comparisons of the ultimate strengths (P_{FEA}), stress contour plots, and load-axial displacement curves. Tables 10–15 provide the ultimate strengths (P_{FEA}) of the FE specimens. Figs. 17–19 display the stress contour plots of the FE specimens with axial lengths of 900, 1500, and 2000 mm ($t = 1.0$ mm) under ultimate load conditions, as well as a comparison with the load-axial displacement curves of the FE specimens. In the legends, K_{as} represents the slope of the initial segment of the load-axial displacement curve, characterising the axial stiffness of the specimen. The introduction of holes resulted in a reduced load-bearing capacity, primarily attributed to a decrease in axial stiffness. Furthermore, the negative impact of the holes on the load-bearing capability

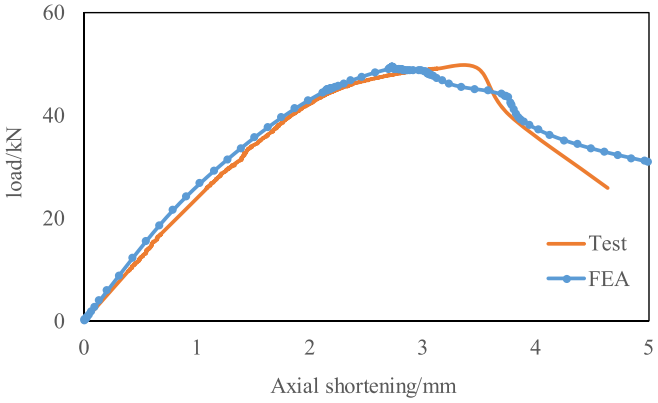

(a) Specimen C1L1500-W1

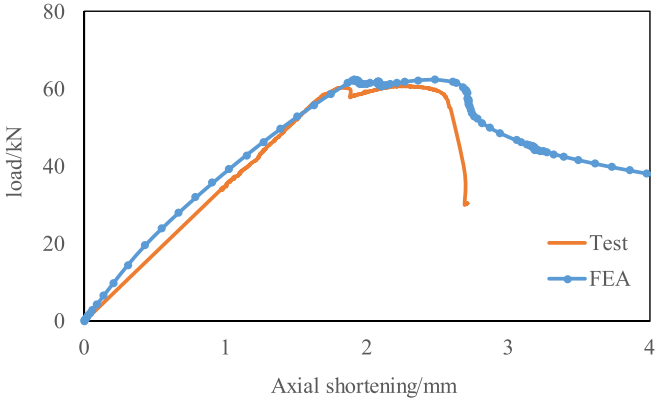

(b) Specimen C1L900

Fig. 15. Load versus axial shortening curves.

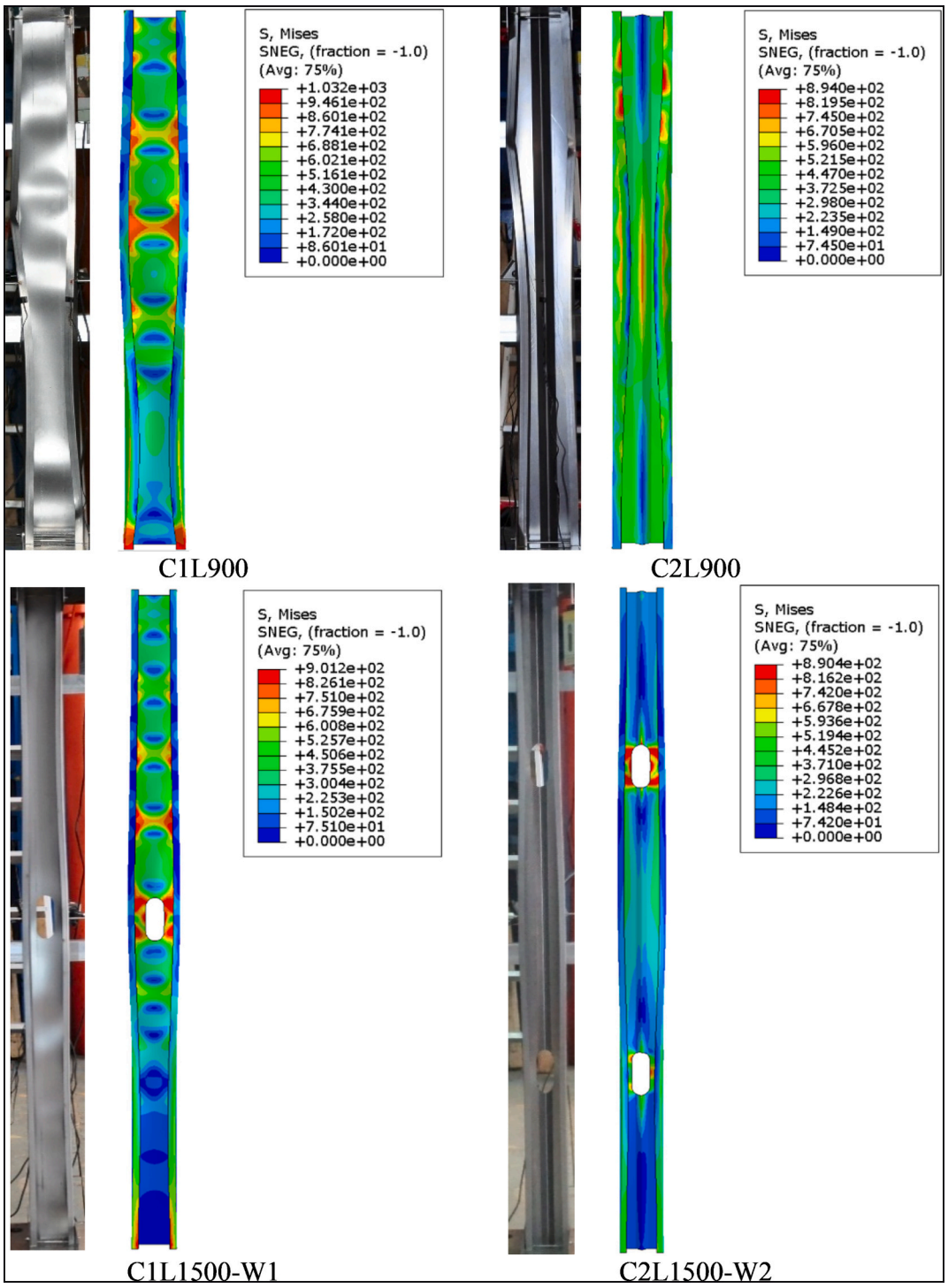

Fig. 16. Comparison of finite element models and the test specimens.

decreased as the component length increased.

Hole impact for flat web members (C1-section): The introduction of holes in the web had a minor effect on the load-bearing capacity of the members. For axial lengths of 300, 900, 1500, and 2000 mm, FE specimens with one hole exhibited load-bearing capacity reductions of 6.8%, 3.7%, 2.8%, and 1.1%, respectively. With five holes at lengths of 1500 and 2000 mm, reductions were 6.7% and 5.6%.

Examining the load-displacement curves in Figs. 17–19, it is evident that while the hole disrupted localised buckling deformations, the stress distribution around the web hole remained almost identical to that without a hole. Furthermore, it can be observed that the slope of the load-displacement curve for the specimens with holes also remained almost unaltered. Therefore, it can be concluded that, for C1-section specimens, the introduction of holes in the web disrupted the continuity of local buckling deformation, resulting in a slight decrease in the post-buckling capacity and a minor reduction in load-bearing capacity.

Hole impact for web-stiffened members (C2-section): The C2-section specimens experienced a relatively significant decrease in load-bearing capacity following the introduction of holes. Load-bearing capacities dropped by 28.9%, 17.5%, 23.1%, and 11.5%, respectively, after a single hole in FE specimens with the corresponding axial length of 300, 900, 1500, and 2000 mm. For specimens with five holes, reductions

Table 9
Range of parameters of C1- and C2-section columns selected for parametric studies.

C1 (t = 0.6 mm,t = 1.0 mm,t = 2.0 mm)	L = 300 mm	NH,W1,F1W1	9 specimens
	L = 900 mm	NH,W1,W2,W3, F1W1	15 specimens
	L = 1500 mm	NH,W1,W2,W3,W5, F1W1,F2W2	21 specimens
	L = 2000 mm	NH,W1,W2,W3,W5, F1W1,F2W2	21 specimens
C2 (t = 0.6 mm,t = 1.0 mm,t = 2.0 mm)	L = 300 mm	NH,W1,F1W1	9 specimens
	L = 900 mm	NH,W1,W2,W3, F1W1	15 specimens
	L = 1500 mm	NH,W1,W2,W3,W5, F1W1,F2W2	21 specimens
	L = 2000 mm	NH,W1,W2,W3,W5, F1W1,F2W2	21 specimens
sum			132specimens

Table 10
Comparison of FE failure loads with codified compression resistance predictions for C1-section specimens (t = 0.6 mm).

Specimen ID	P_{FEA}	P_{DSM}	P^{M}_{DSM}	P_{FEA}/P_{DSM}	P_{FEA}/P^{M}_{DSM}
C1L300	31.4	31.3	31.8	1.00	0.99
C1L300-W1	31.6	31.2	29.9	1.01	1.06
C1L300-F1W1	26.6	27.6	25.1	0.96	1.06
C1L900	26.6	25.6	26.1	1.04	1.02
C1L900-W1	25.0	25.4	25.7	0.98	0.97
C1L900-W2	24.4	25.3	25.3	0.97	0.96
C1L900-W3	23.7	25.2	24.5	0.94	0.97
C1L900-F1W1	22.3	22.4	23.7	1.00	0.94
C1L1500	19.6	17.1	17.6	1.14	1.11
C1L1500-W1	19.8	16.8	17.3	1.18	1.15
C1L1500-W2	19.2	16.7	17.2	1.15	1.11
C1L1500-W3	18.4	16.6	17.1	1.11	1.08
C1L1500-W5	18.2	16.3	16.6	1.11	1.10
C1L1500-F1W1	19.2	14.8	16.4	1.30	1.17
C1L1500-F2W2	18.4	14.7	15.8	1.25	1.16
C1L2000	14.9	12.0	12.3	1.25	1.21
C1L2000-W1	14.8	11.8	12.2	1.25	1.21
C1L2000-W2	14.6	11.7	12.1	1.25	1.21
C1L2000-W3	15.1	11.6	12.1	1.29	1.25
C1L2000-W5	14.3	11.5	11.9	1.24	1.20
C1L2000-F1W1	14.6	10.3	11.6	1.42	1.27
C1L2000-F2W2	14.4	10.2	11.4	1.41	1.26
			P_m	1.15	1.11
			COV	0.13	0.09

were 29.5% and 21.8%.

A noticeable decline in slope in the load-displacement curve for C2-sections is indicative of a reduced axial stiffness, along with a significant drop in the stress levels around the hole and along the stiffened parts of the web, as shown in Figs. 17–19. It was found that the hole has weakened the axial stiffness of the specimen, attributed to a significant reduction in its load-bearing capacity.

Web and Flange Hole Impact: The inclusion of holes in both the web and flange further reduced the load-bearing capacity. For C1-section medium-short columns (L = 900 mm), this impact resulted in an extra 9.3% reduction, while for medium-long columns (L = 1500 mm), it was 3.5%. For equivalent C2-section specimens, the additional reductions were 17.4% and 6.9%. It is worth noting that the decrease in load-bearing capacity does not entirely align with the trend of reduced axial stiffness of the member. Figs. 20 and 21 illustrate increased stress around the hole in the web and near the flange, along with a larger area of localised deformation. This observation implies that the existence of holes in both the web and flange at the same height may yield detrimental mutual influence, ultimately resulting in a more substantial reduction in load-bearing capacity.

Table 11
Comparison of FE failure loads with codified compression resistance predictions for C1-section specimens (t = 1.0 mm).

Specimen ID	P_{FEA}	P_{DSM}	P^{M}_{DSM}	P_{FEA}/P_{DSM}	P_{FEA}/P^{M}_{DSM}
C1L300	83.2	76.4	78.3	1.09	1.06
C1L300-W1	77.6	74.4	72.3	1.04	1.07
C1L300-F1W1	63.5	62.0	60.7	1.02	1.05
C1L900	62.4	62.4	64.2	1.00	0.97
C1L900-W1	60.1	60.2	61.7	1.00	0.97
C1L900-W2	59.9	59.9	60.8	1.00	0.99
C1L900-W3	57.8	59.6	59.2	0.97	0.98
C1L900-F1W1	54.3	50.2	57.4	1.08	0.95
C1L1500	50.7	41.8	43.3	1.21	1.17
C1L1500-W1	49.3	39.6	41.8	1.24	1.18
C1L1500-W2	48.3	39.3	41.6	1.23	1.16
C1L1500-W3	46.9	39.0	41.2	1.20	1.14
C1L1500-W5	47.3	38.4	40.0	1.23	1.18
C1L1500-F1W1	47.5	33.1	39.7	1.43	1.20
C1L1500-F2W2	45.4	32.9	38.2	1.38	1.19
C1L2000	35.8	29.0	30.5	1.23	1.18
C1L2000-W1	35.4	27.4	29.4	1.29	1.21
C1L2000-W2	35.3	27.2	29.3	1.30	1.20
C1L2000-W3	34.8	27.0	29.1	1.29	1.19
C1L2000-W5	33.8	26.7	28.7	1.27	1.18
C1L2000-F1W1	35.3	23.0	27.9	1.54	1.27
C1L2000-F2W2	34.4	22.9	27.5	1.50	1.25
			P_m	1.21	1.12
			COV	0.14	0.09

Table 12
Comparison of FE failure loads with codified compression resistance predictions for C1-section specimens (t = 2 mm).

Specimen ID	P_{FEA}	P_{DSM}	P^{M}_{DSM}	P_{FEA}/P_{DSM}	P_{FEA}/P^{M}_{DSM}
C1L300	255.5	250.8	245.7	1.02	1.04
C1L300-W1	222.4	232.7	217.1	0.96	1.02
C1L300-F1W1	175.8	188.5	182.4	0.93	0.96
C1L900	195.8	204.3	204.1	0.96	0.96
C1L900-W1	174.8	187.5	187.9	0.93	0.93
C1L900-W2	167.2	186.5	185.1	0.90	0.90
C1L900-W3	170.9	185.6	180.4	0.92	0.95
C1L900-F1W1	145.7	152.4	175.6	0.96	0.83
C1L1500	144.9	139.1	138.1	1.04	1.05
C1L1500-W1	141.3	115.3	127.5	1.23	1.11
C1L1500-W2	139.8	113.8	126.8	1.23	1.10
C1L1500-W3	137.6	112.4	125.7	1.22	1.09
C1L1500-W5	132.7	109.5	122.1	1.21	1.09
C1L1500-F1W1	132.6	102.4	121.1	1.29	1.09
C1L1500-F2W2	131.9	101.6	116.7	1.30	1.13
C1L2000	94.7	88.2	88.2	1.07	1.07
C1L2000-W1	93.4	69.4	81.5	1.35	1.15
C1L2000-W2	94.5	68.7	81.3	1.37	1.16
C1L2000-W3	92.0	68.1	80.9	1.35	1.14
C1L2000-W5	89.4	66.7	79.6	1.34	1.12
C1L2000-F1W1	95.1	62.7	77.4	1.52	1.23
C1L2000-F2W2	92.1	62.1	76.4	1.48	1.21
			P_m	1.16	1.06
			COV	0.17	0.10

Impact of Strength Grade on Structural Performance: The strength comparison for finite element analysis (FEA) specimens of CP980, G500, and Q235 is detailed in Tables 17 and 18, where P^{CP980}_{FEA}, P^{G500}_{FEA} and P^{Q235}_{FEA} represent the ultimate strengths of the FEA specimens. On average, the ratios of $P^{CP980}_{FEA}/P^{G500}_{FEA}$ are 1.15 and 1.19 for C1-section and C2-section, respectively. Similarly, the mean ratios of $P^{CP980}_{FEA}/P^{Q235}_{FEA}$ are 1.62 and 1.69 for the C1-section and the C2-section, respectively. The comparison results indicate that using the advanced high-strength steel CP980 results in an average increase in ultimate load-bearing capacity of 15% and 19% compared to high-strength steel G500, and 62% and 69% compared to Q235. It can be also found in Tables 17 and 18 that the enhancement in load-bearing capacity diminishes with the increase of the specimen length. The load-bearing capacity ratios for

Table 13
Comparison of FE failure loads with codified compression resistance predictions for C2-section specimens (t = 0.6 mm).

Specimen ID	P_{FEA}	P_{DSM}	P^{M}_{DSM}	P_{FEA}/P_{DSM}	P_{FEA}/P^{M}_{DSM}
C2L300	53.2	45.4	44.7	1.17	1.19
C2L300-W1	31.1	31.3	29.3	0.99	1.06
C2L300-F1W1	29.1	22.0	24.6	1.32	1.18
C2L900	45.5	45.4	39.0	1.00	1.17
C2L900-W1	25.3	25.8	28.4	0.98	0.89
C2L900-W2	23.3	25.6	27.3	0.91	0.85
C2L900-W3	23.5	25.4	25.5	0.92	0.92
C2L900-F1W1	21.8	18.2	26.4	1.20	0.83
C2L1500	27.5	34.3	29.2	0.80	0.94
C2L1500-W1	21.1	17.6	21.4	1.20	0.98
C2L1500-W2	20.4	17.3	21.2	1.17	0.96
C2L1500-W3	18.9	17.1	20.7	1.11	0.92
C2L1500-W5	18.7	16.6	19.1	1.12	0.98
C2L1500-F1W1	20.1	12.4	20.4	1.62	0.99
C2L1500-F2W2	18.3	12.4	19.5	1.48	0.94
C2L2000	20.4	23.6	21.2	0.86	0.96
C2L2000-W1	17.3	12.2	15.6	1.41	1.11
C2L2000-W2	16.3	12.1	15.5	1.34	1.05
C2L2000-W3	15.2	12.0	15.3	1.27	1.00
C2L2000-W5	14.5	11.7	14.6	1.24	0.99
C2L2000-F1W1	16.7	8.7	14.8	1.92	1.13
C2L2000-F2W2	15.4	8.7	14.5	1.78	1.06
			P_m	1.22	1.01
			COV	0.24	0.10

Table 14
Comparison of FE failure loads with codified compression resistance predictions for C2-section specimens (t = 1.0 mm).

Specimen ID	P_{FEA}	P_{DSM}	P^{M}_{DSM}	P_{FEA}/P_{DSM}	P_{FEA}/P^{M}_{DSM}
C2L300	110.4	104.6	102.7	1.06	1.07
C2L300-W1	78.5	73.0	70.2	1.08	1.12
C2L300-F1W1	66.4	53.8	59.0	1.23	1.13
C2L900	79.2	104.6	88.5	0.76	0.89
C2L900-W1	65.3	60.0	67.2	1.09	0.97
C2L900-W2	56.5	59.5	64.6	0.95	0.87
C2L900-W3	58.8	59.0	60.4	1.00	0.97
C2L900-F1W1	51.5	44.3	62.5	1.16	0.82
C2L1500	65.7	80.5	64.3	0.82	1.02
C2L1500-W1	50.5	40.8	49.2	1.24	1.03
C2L1500-W2	46.8	40.3	48.5	1.16	0.97
C2L1500-W3	45.6	39.7	47.4	1.15	0.96
C2L1500-W5	46.4	38.6	43.9	1.20	1.06
C2L1500-F1W1	46.0	30.3	46.7	1.52	0.99
C2L1500-F2W2	41.9	30.2	44.6	1.39	0.94
C2L2000	42.1	46.4	43.6	0.91	0.97
C2L2000-W1	37.3	28.4	33.4	1.32	1.12
C2L2000-W2	35.2	28.1	33.2	1.26	1.06
C2L2000-W3	33.9	27.7	32.7	1.22	1.04
C2L2000-W5	33.0	27.1	31.4	1.21	1.05
C2L2000-F1W1	35.7	21.2	31.7	1.68	1.13
C2L2000-F2W2	33.2	21.1	31.2	1.57	1.06
			P_m	1.18	1.01
			COV	0.19	0.08

specimens with holes are considerably higher than those without holes at the same axial length, indicating that a slower reduction in load-bearing capacity for CP980 specimens with holes compared to those made from G500 and Q235. This might be attributed to the fact that the high yield and tensile strengths of CP980 allow the areas around holes in the plate to endure greater stress concentration level. Overall, the comparisons in Tables 17 and 18 indicate that, for axially compressed thin-walled specimens with holes, using advanced high-strength steel is capable of providing significant advantages in axial capacity enhancement as well as lower strength reduction when perforations are present.

It is worth noting that the yield strength of the advanced high-strength steel has not been fully realized across the cross-sections of the members investigated herein. Therefore, ongoing research is being

Table 15
Comparison of FE failure loads with codified compression resistance predictions for C2-section specimens (t = 2.0 mm).

Specimen ID	P_{FEA}	P_{DSM}	P^{M}_{DSM}	P_{FEA}/P_{DSM}	P_{FEA}/P^{M}_{DSM}
C2L300	283.6	281.2	275.4	1.01	1.03
C2L300-W1	234.1	228.7	205.1	1.02	1.14
C2L300-F1W1	183.8	176.2	172.3	1.04	1.07
C2L900	268.2	281.2	232.3	0.95	1.15
C2L900-W1	185.2	187.2	192.2	0.99	0.96
C2L900-W2	161.7	185.6	185.0	0.87	0.87
C2L900-W3	163.2	184.0	173.0	0.89	0.94
C2L900-F1W1	144.9	144.8	178.7	1.00	0.81
C2L1500	153.3	163.8	156.7	0.94	0.98
C2L1500-W1	133.2	124.0	130.7	1.07	1.02
C2L1500-W2	124.4	121.5	128.9	1.02	0.96
C2L1500-W3	126.5	119.1	126.0	1.06	1.00
C2L1500-W5	127.3	113.9	116.7	1.12	1.09
C2L1500-F1W1	126.3	101.1	124.1	1.25	1.02
C2L1500-F2W2	120.5	100.6	118.6	1.20	1.02
C2L2000	94.2	92.8	92.8	1.02	1.02
C2L2000-W1	89.3	70.3	77.5	1.27	1.15
C2L2000-W2	87.2	69.9	76.9	1.25	1.13
C2L2000-W3	85.1	69.5	76.0	1.22	1.12
C2L2000-W5	85.6	68.7	72.9	1.25	1.17
C2L2000-F1W1	87.9	63.6	73.6	1.38	1.19
C2L2000-F2W2	84.6	63.2	72.3	1.34	1.17
			P_m	1.10	1.05
			COV	0.13	0.10

conducted to explore optimal section designs, aiming to fully harness the advantages associated with the high yield strength inherent in advanced high-strength steel.

5. Design calculation for column with holes

5.1. The current direct strength method

The direct strength method (DSM) is a load-bearing calculation method for thin-walled members adopted by AISI S100–16 [5]. Compared to the Effective Width Method, the Direct Strength Method offers a more straightforward calculation process. In DSM, the nominal axial strength (P_n) for a thin-walled axial compression member is determined as the lowest among its nominal axial strengths for overall buckling (P_{ne}), local buckling (P_{nl}), and distortional buckling (P_{nd}). The equations for overall buckling, local buckling and distortional buckling of the direct strength method are presented as follows:

$$P_{ne} = \begin{cases} \left(0.658^{\lambda_c^2}\right) P_y & \lambda_c \le 1.5 \\ \left(\dfrac{0.877}{\lambda_c^2}\right) P_y & \lambda_c > 1.5 \end{cases} \tag{1}$$

$$P_{nl} = \begin{cases} P_{ne} & \lambda_l \le 0.776 \\ \left[1 - 0.15\left(\dfrac{P_{crl}}{P_{ne}}\right)^{0.4}\right]\left(\dfrac{P_{crl}}{P_{ne}}\right)^{0.4} P_{ne} & \lambda_l > 0.776 \end{cases} \tag{2}$$

$$P_{nd} = \begin{cases} P_y & \lambda_d \le 0.561 \\ \left[1 - 0.25\left(\dfrac{P_{crd}}{P_y}\right)^{0.6}\right]\left(\dfrac{P_{crd}}{P_y}\right)^{0.6} P_y & \lambda_d > 0.561 \end{cases} \tag{3}$$

where: $\lambda_c = \sqrt{P_y/P_{cre}}$, $P_y = A_g f_y$; $\lambda_l = \sqrt{P_{ne}/P_{crl}}$, $P_{crl} = A_g f_{crl}$; $\lambda_d = \sqrt{P_y/P_{crd}}$, $P_{crd} = A_g f_{crd}$. A_g is the gross cross-section area and f_y is the 0.2% proof stress (yield stress) of the material. The elastic flexural buckling strength (P_{cre}) is calculated as $P_{cre} = A_g \pi^2 EI/(KL)^2$, and the computation of the elastic local buckling stress (f_{crl}) and distortional buckling stress (f_{crd}) were obtained from a rational elastic finite strip buckling analysis.

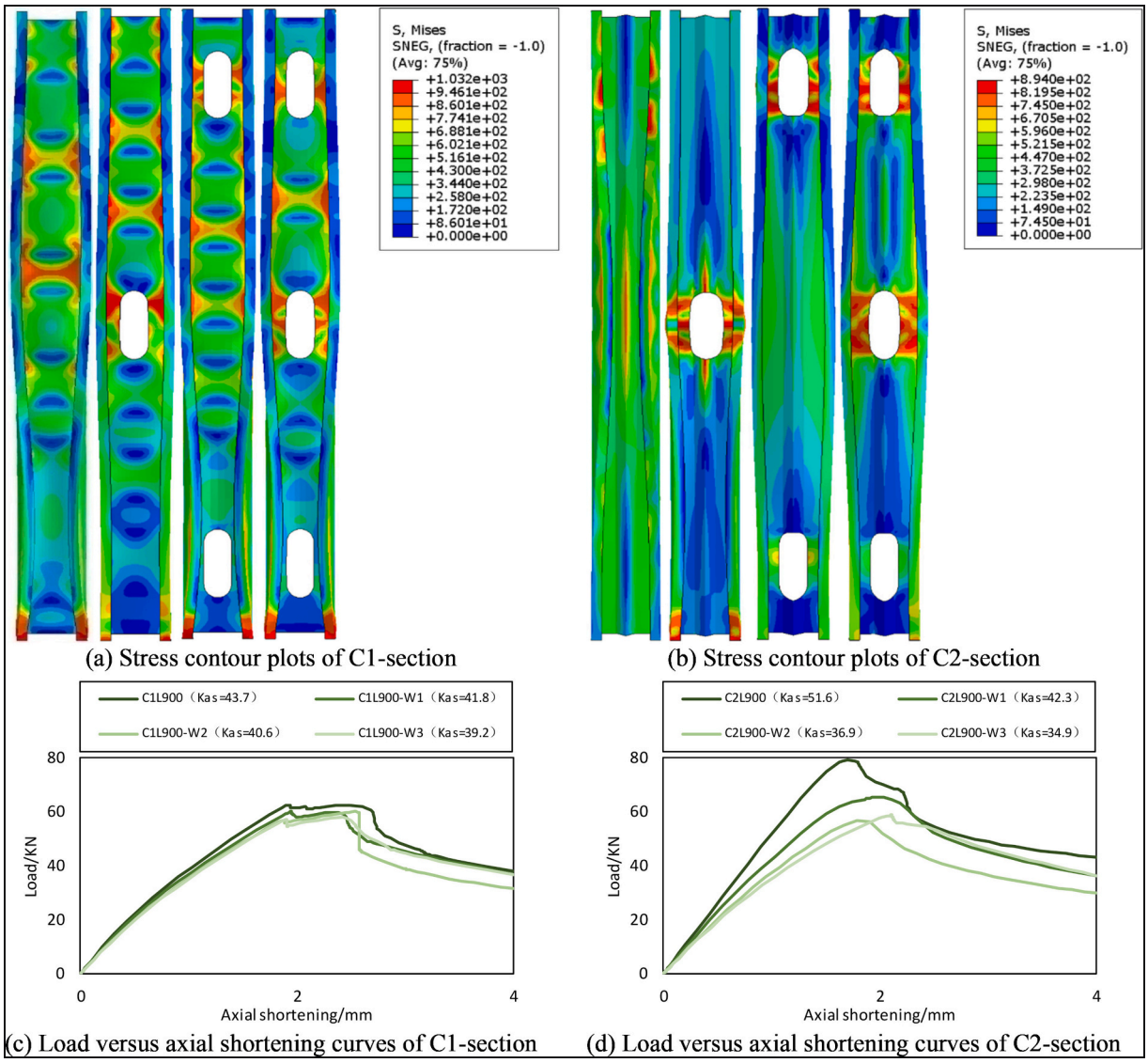

Fig. 17. Effects of web holes on the ultimate strengths for thin-walled open section columns (L = 900 mm).

For perforated thin-walled columns, DSM incorporates the impact of these holes on the overall buckling strength (P_{ne}^{H}), local buckling strength (P_{nl}^{H}), and distortional buckling strength (P_{nd}^{H}) of the members. In the calculation of the overall buckling strength of perforated specimens, the expression for the strength curve remains consistent with that for specimens without holes. The influence of the holes is factored in using a weighted method to adjust the elastic flexural buckling strength, which for perforated member is represented as P_{cre}^{H}. In the calculation of the local buckling strength of perforated specimens, the strength curve for local buckling is as shown in Eq. (4), where $P_{net} = A_{net}f_y$, in which A_{net} is the net cross-sectional area at the hole location, and $P_{crl}$is the minimum value between the elastic local buckling strength of the specimen without a hole and the elastic local buckling strength of the perforated specimen, as detailed in Commentary on AISI S100–16 [25]. The calculation curve for the distortional buckling strength of perforated specimens is presented in Eq. (5),

$$P_{nl}^{H} = \begin{cases} P_{ne} & \lambda_l \le 0.776 \\ \left[1 - 0.15\left(\frac{P_{crl}}{P_{ne}}\right)^{0.4}\right]\left(\frac{P_{crl}}{P_{ne}}\right)^{0.4} & \lambda_l > 0.776 \end{cases} \quad \text{and } P_{nl}^{H} \le P_{ynet} \tag{4}$$

$$P_{nd}^{H} = \begin{cases} P_{ynet} & \lambda_d \le \lambda_{d1} \\ P_{ynet} - \left[\frac{P_{ynet} - P_{d2}}{\lambda_{d2} - \lambda_{d1}}\right](\lambda_d - \lambda_{d1}) & \lambda_{d1} < \lambda_d \le \lambda_{d2} \\ \left[1 - 0.25\left(\frac{P_{crd}}{P_y}\right)^{0.6}\right]\left(\frac{P_{crd}}{P_y}\right)^{0.6} P_y & \lambda_d > \lambda_{d2} \end{cases} \tag{5}$$

where $\lambda_{d1} = 0.561(P_{ynet}/P_y)$, $\lambda_{d2} = 0.561\left[14(P_{ynet}/P_y)^{0.4} - 13.0\right]$, and $P_{d2} = \left[1 - 0.25(1/\lambda_{d2})^{1.2}\right](1/\lambda_{d2})^{1.2}P_y$.

The nominal design strength of axially compressed column obtained by DSM for perforated thin-walled columns is presented as P_{DSM}. The column strength determined by finite element analysis (P_{FEA}) and tests (P_{Test}) were used to evaluate the design strength (P_{DSM}). The statistical comparisons are presented in Tables 10–16. For the C1-section specimens with thicknesses t of 0.6, 1.0, and 2.0 mm, the mean values for P_{FEA}/P_{DSM} are 1.15, 1.21, and 1.16, respectively, with corresponding COVs of 0.13, 0.14, and 0.17. For the C2-section specimens with thicknesses t of 0.6, 1.0, and 2.0 mm, the mean values for P_{FEA}/P_{DSM} are 1.22, 1.18, and 1.10, respectively, paired with COVs of 0.24, 0.19, and 0.13. Moreover, the mean value of P_{Test}/P_{DSM} is 1.07 and a COV of 0.17.

The comparison reveals that the DSM ultimate capacity predictions

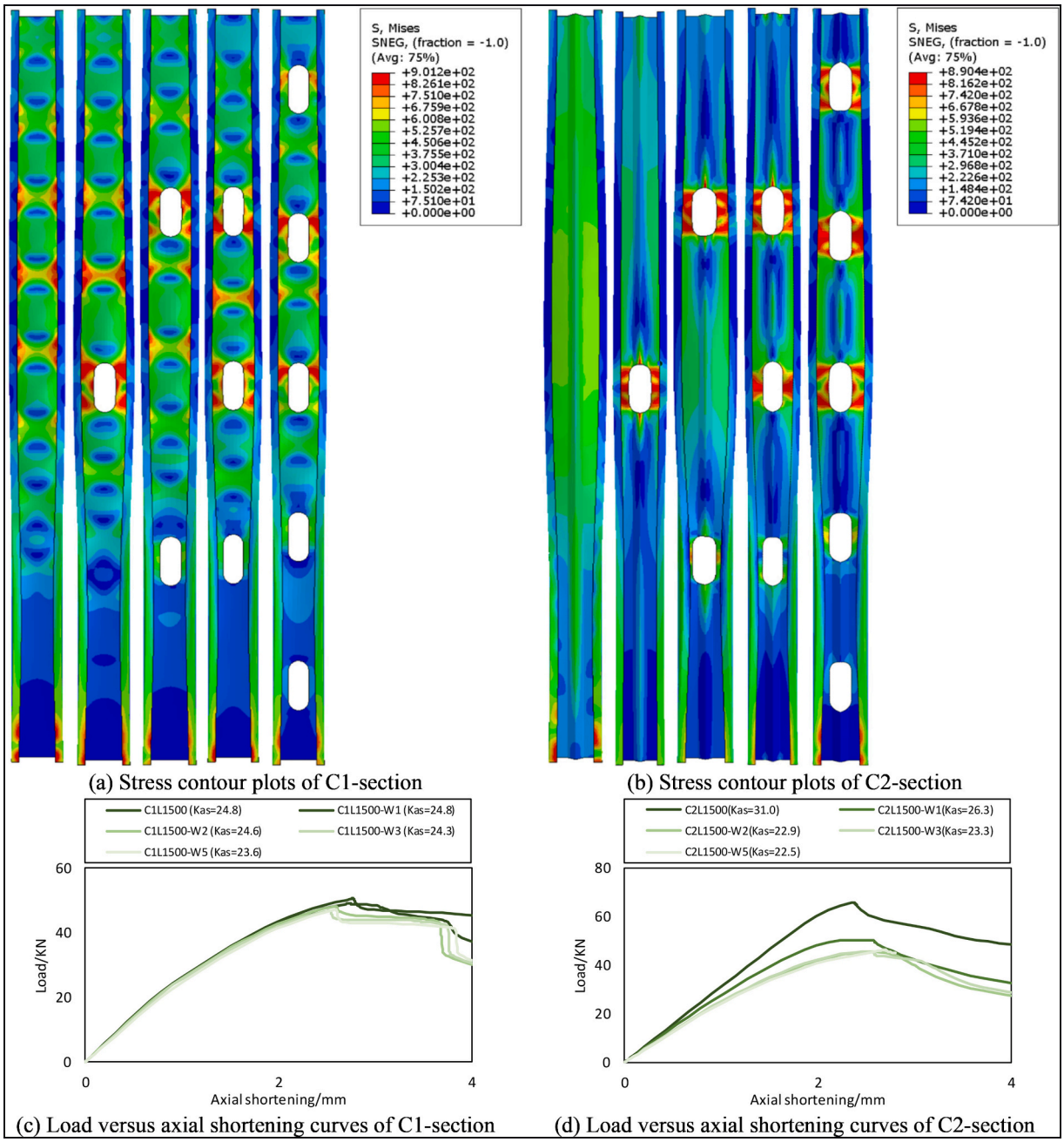

Fig. 18. Effects of web holes on the ultimate strengths for thin-walled open section columns (L = 1500 mm).

are generally conservative, albeit with a high degree of scatter. For columns featuring a web stiffener, there is a discernible disparity in load-carrying capacity calculations. This disparity becomes more pronounced as the length of the specimen increases, leading to even greater conservatism in the DSM predictions.

The conservative and highly scattered design predictions from DSM can be attributed to: 1) potential inaccuracies in design calculations for columns without perforations; 2) overestimation or underestimation of the impact of holes on load-bearing capacity in the calculations.

5.2. Modified direct strength method

In this study, the DSM design rules are modified to attain more accurate and consistent column design predictions for the examined perforated channel columns. The modifications were made by reevaluating the design calculations for non-perforated members and reassessing the influence of holes on load-bearing capacity for perforated members.

It is observed in Tables 19 and 20 that, compared to FE results, the design strengths by DSM for the C1-section are conservative, while those for the C2-section are overestimated. The reduction in load-bearing capacity for perforated members was evaluated based on the FE results, alongside the reduction obtained from the design strength calculated using the DSM, as depicted in Fig. 22, where the load-bearing reduction factor R, indicating the ratio of the load-bearing capacity of the perforated member to the non-perforated one, is plotted against the number of holes in the web. The comparison reveals that the reduction in strength of perforated members calculated using the DSM exceeds the FE values, with this trend being more pronounced in the C2-section. Therefore, the modified design calculation for the perforated member was divided into three steps: firstly, the precise determination of load-bearing capacity when the member is unperforated; secondly, the

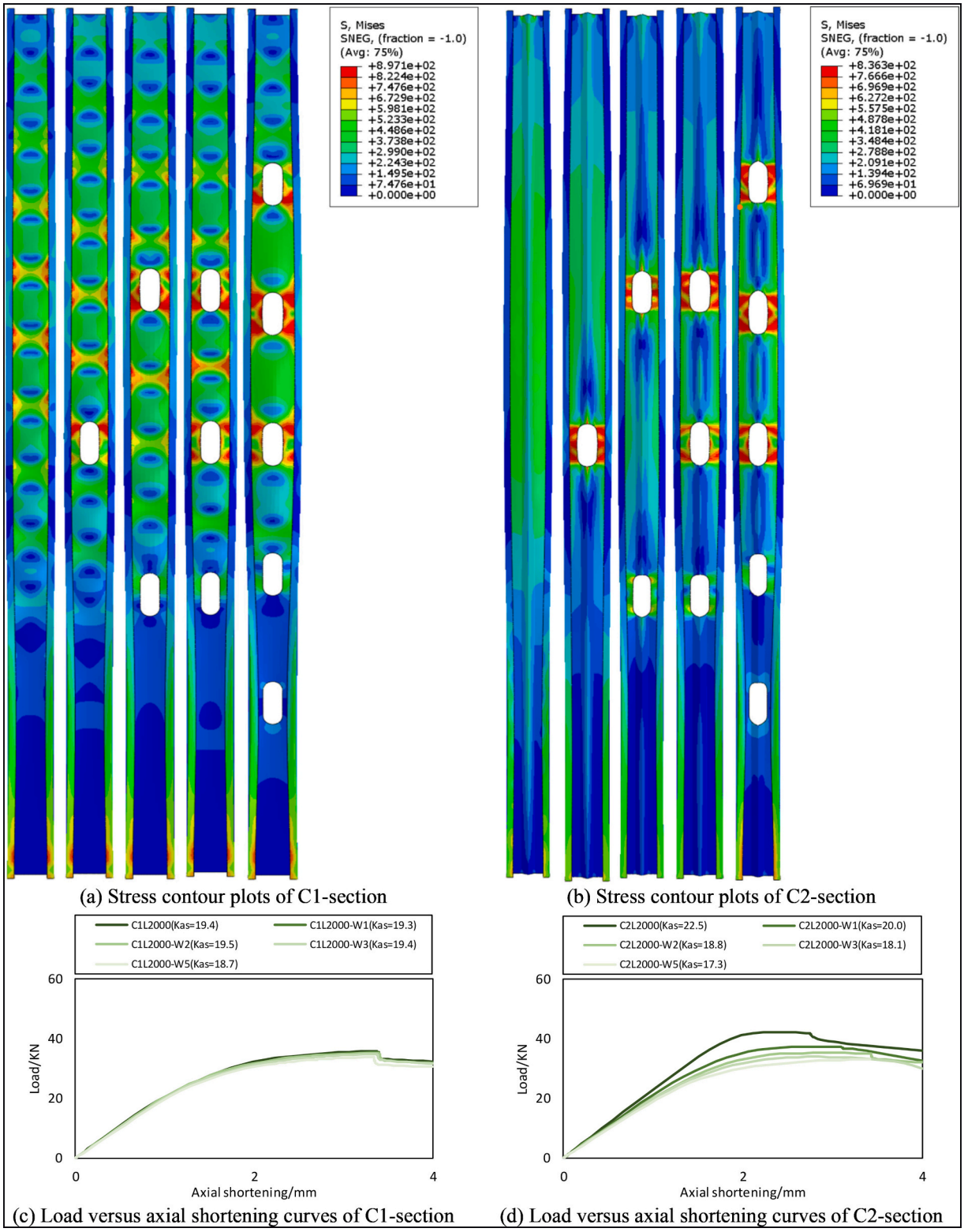

Fig. 19. Effects of web holes on the ultimate strengths for thin-walled open section columns (L = 2000 mm).

derivation of the load-bearing reduction factor based on hole location, number, and geometric dimensions; and thirdly, the multiplication of the reduction factor by the load-bearing capacity value calculated for the non-perforated member.

In the load-bearing capacity calculation of the non-perforated member, the local buckling strength curve and distortion buckling strength curve were revised to Eqs. (6) and (7), respectively. The local buckling strength curve simply adjusts the coefficient parameter from 0.15 to 0.1, while the non-dimensional slenderness ratio (λ_l) threshold is changed to 0.861. In the distortion buckling strength curve, the yield strength is replaced with the overall buckling strength value to account for the interaction of distortion and overall buckling. The modified design strength of the non-perforated member is P_n. As shown in Tables 19 and 20, the modified calculations for the non-perforated columns

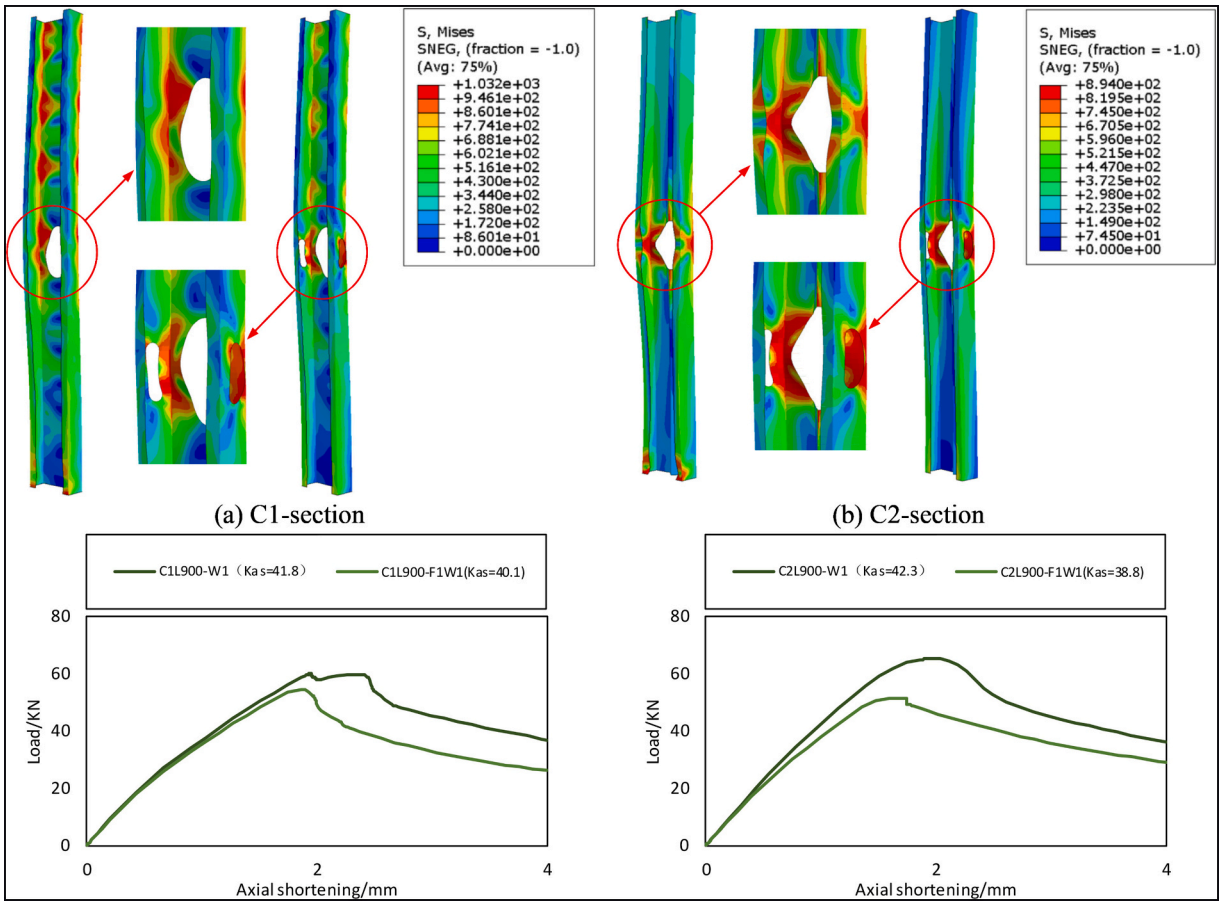

Fig. 20. Stress contour plots of 900 mm specimens with web and flange holes.

are shown to be more accurate and less scattered than the DSM calculations.

$$P_{nl} = \begin{cases} P_{ne} & \lambda_l \le 0.861 \\ \left[1 - 0.1\left(\frac{P_{crl}}{P_{ne}}\right)^{0.4}\right]\left(\frac{P_{crl}}{P_{ne}}\right)^{0.4} P_{ne} & \lambda_l > 0.861 \end{cases} \tag{6}$$

$$P_{nd} = \begin{cases} P_{ne} & \lambda_d \le 0.561 \\ \left[1 - 0.25\left(\frac{P_{crd}}{P_{ne}}\right)^{0.6}\right]\left(\frac{P_{crd}}{P_{ne}}\right)^{0.6} P_{ne} & \lambda_d > 0.561 \end{cases} \tag{7}$$

The modified calculation for the perforated members is represented as $P_n^{hole} = R_W R_F P_n$, in which $R_W = K_{L+G}K_D K_t$ is the strength reduction factor for the perforated web. The parameter K_{L+G} indicates the impact of web perforation on local buckling and overall buckling strength, K_D indicates the effect of web perforation on distortional buckling strength, and K_t is the thickness adjustment coefficient. The expressions for K_{L+G}, K_D, and K_t are given by Eqs. (8)–(10), where L_H is the hole length, W_H is the hole width, L is the axial length of a column, $W$is the width of the web, and t represents the thickness of the plate. If there are multiple holes, the cumulative hole length is used for calculations.

$$K_{L+G} = \begin{cases} 1 - 0.4\left(\frac{\sum L_H}{L}\right)^2 & \text{flat web section} \\ 0.8 - 0.8\left(\frac{\sum L_H}{L}\right)^2 & \text{web-stiffened section} \end{cases} \tag{8}$$

$$K_D = 1 - 0.4\left(\frac{\sum W_H}{W}\right)^2 \tag{9}$$

$$K_t = \begin{cases} \left(\frac{3}{2+t}\right)^{0.15} & \text{flat web section} \\ \left(\frac{3}{2+t}\right)^{-0.3} & \text{web-stiffened section} \end{cases} \tag{10}$$

Similar to the expression structure of R_W, the strength reduction factor for the perforated web is $R_F = K_{L+G}K_D$, in which K_{L+G} indicates the impact of the web perforation on local buckling and overall buckling strength, and K_D indicates the effect of the web perforation on distortional buckling strength. The expressions for K_{L+G} and K_D are given by Eqs. (11) and (12), respectively, where L_H is the hole length, W_H is the hole width, L is the axial length of the component, and F is the width of the flange. If multiple holes are drilled axially, the cumulative hole length is used for calculations.

$$K_{L+G} = 1 - \left(\frac{\sum L_H}{L}\right)^{1.2} \tag{11}$$

$$K_D = 1 - 0.4\left(\frac{\sum W_H}{F}\right)^{0.2} \tag{12}$$

The strength reduction factors for perforated columns are shown in Fig. 22. For the C1-section, the trend of the proposed reduction factor is closer to the decay trend of the finite element data. For the C2-section, the proposed reduction factor significantly outperforms the reduction factor obtained from DSM calculations and is also closer to the FE data.

The proposed strength reduction factor for the perforated section is multiplied by the load-bearing capacity of the non-perforated specimen to obtain the modified design strength for the perforated specimen, represented as P_{DSM}^M Tables 10–16 detail the ratios of P_{FEA}/P_{DSM}^M and

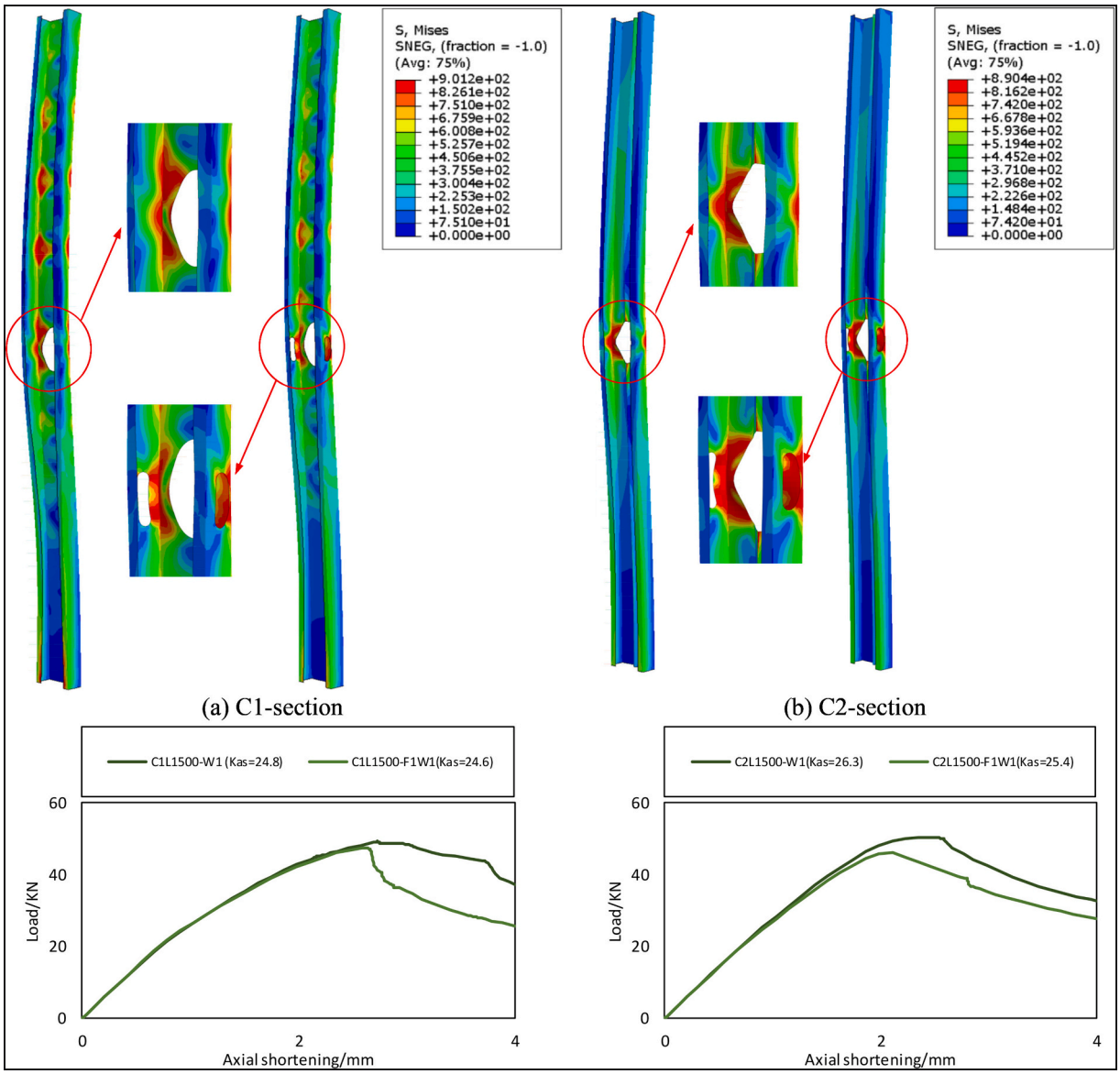

Fig. 21. Stress contour plots of 1500 mm specimens with web and flange holes.

P_{Test}/P^{M}_{DSM}. In the C1-section specimens, with thicknesses t = 0.6, 1.0, and 2.0 mm, the mean values ofP_{FEA}/P^{M}_{DSM} are 1.11, 1.12, and 1.06, with COVs of 0.09, 0.09, and 0.10, respectively. Regarding the C2-section specimens with thicknesses t = 0.6, 1.0, and 2.0 mm, the mean values of $P_{FEA}/P^{M}_{DSM}$are 1.01, 1.01, and 1.05, respectively, with COVs of 0.10, 0.08, and 0.10. The ratio of P_{Test}/P^{M}_{DSM} is shown in Table 15, with a mean value of 1.02 and a COV of 0.11. Compared to the current DSM, the modified method provides more accurate and less scattered axial capacity predictions. Furthermore, the revised calculation approach removes the necessity to independently evaluate the impacts of perforations on local, distortional, and overall buckling strengths, simplifying the computation process and enhancing its user-friendliness.

6. Conclusions

In this study, laboratory testing and numerical modeling have been conducted to investigate the effects of perforation quantity and location on the buckling instability and ultimate load-bearing capacity of high strength steel CP980 channel section axial compression members. A total of 19 column tests were performed on two channel sections with varying lengths. Parametric studies were also conducted, generating 132 additional results over an extended range of thicknesses, member lengths, and perforations. The combined test and FE data was used to assess the appropriateness of the DSM for perforated members and modifications to current DSM were also proposed. Key findings and implications are as follows:

1. Flat Web Members (C1-section): After perforation, these members typically experienced local buckling or the interaction of local and overall buckling. Perforations on the web primarily impacted post-local buckling strength, causing a minor loss in load-bearing capacity.
2. Web-Stiffened Members (C2-section): Distortional buckling and the interaction of distortional and overall buckling were observed for these members once perforated. The most significant loss in load-bearing capacity post-perforation was primarily due to disruptions at the stiffened regions, which notably decreased axial stiffness.
3. Perforation Impact on Both Web and Flanges: There was a higher stress level around the holes and a broader boundary of localised deformation. Deformations from holes in both the web and flange at

Table 16
Comparison of test failure loads with codified compression resistance predictions for C1- and C2-section specimens (t = 1.0 mm).

Specimen ID	P_{Test}	P_{DSM}	P^{M}_{DSM}	P_{Test}/P_{DSM}	P_{Test}/P^{M}_{DSM}
C1L300	82.20	76.4	78.3	1.08	1.05
C1L300R1	80.52	76.4	78.3	1.05	1.03
C1L300-W1	74.24	74.4	72.3	1.00	1.03
C1L300-W1R	72.38	74.4	72.3	0.97	1.00
C1L300-F1W1	62.41	62	60.7	1.01	1.03
C1L900	60.63	62.4	64.2	0.97	0.94
C1L900R	61.88	62.4	64.2	0.99	0.96
C1L900-W1	55.32	60.2	61.7	0.92	0.90
C1L900-F1W1	48.96	50.2	57.4	0.98	0.85
C1L1500	52.84	41.8	43.3	1.26	1.22
C1L1500-W1	49.12	39.6	41.8	1.24	1.18
C1L1500-W2	47.11	39.3	41.6	1.20	1.13
C1L1500-F1W1	45.73	33.1	39.7	1.38	1.15
C1L1500-F2W2	41.92	32.9	38.2	1.27	1.10
C2L900	76.38	104.6	88.5	0.73	0.86
C2L900-W1	61.35	60	67.2	1.02	0.91
C2L1500	60.58	80.5	64.3	0.75	0.94
C2L1500-W1	54.88	40.8	49.2	1.35	1.12
C2L1500-W2	44.54	40.3	48.5	1.11	0.92
P_m				1.07	1.02
COV				0.17	0.11

Table 17
Comparison of FE failure loads with different strength grade for C1-section specimens (t = 1.0 mm).

Specimen ID	P^{G500}_{FEA}	P^{Q235}_{FEA}	$P^{CP980}_{FEA}/P^{H500}_{FEA}$	$P^{CP980}_{FEA}/P^{Q235}_{FEA}$
C1L300	72.1	47.6	1.15	1.75
C1L300-W1	59.9	37.7	1.30	2.06
C1L300-F1W1	47.3	29.1	1.34	2.18
C1L900	54.5	37.4	1.14	1.67
C1L900-W1	51.5	33.2	1.17	1.81
C1L900-W2	47.5	29.6	1.26	2.02
C1L900-W3	46.7	29.5	1.24	1.96
C1L900-F1W1	41.2	26.4	1.32	2.06
C1L1500	45.9	36.1	1.10	1.40
C1L1500-W1	43.9	32.6	1.12	1.51
C1L1500-W2	43.0	31.9	1.12	1.51
C1L1500-W3	42.6	31.6	1.10	1.48
C1L1500-W5	42.9	31.1	1.10	1.52
C1L1500-F1W1	39.0	26.5	1.22	1.79
C1L1500-F2W2	37.1	26.1	1.22	1.74
C1L2000	34.2	30.2	1.05	1.19
C1L2000-W1	33.7	28.4	1.05	1.25
C1L2000-W2	33.1	27.8	1.07	1.27
C1L2000-W3	33.4	27.0	1.04	1.29
C1L2000-W5	32.0	26.4	1.06	1.28
C1L2000-F1W1	32.7	24.7	1.08	1.43
C1L2000-F2W2	31.3	24.3	1.10	1.42
P_m			1.15	1.62

the same height have a compounded impact, leading to a further reduction in load-bearing capacity at the web-flange junction.

4. Assessment of DSM: The current DSM was found to be inadequate to predict the post-perforation degradation trend in load-bearing capacity, showing a high level of inaccuracy and inconsistency.
5. Proposed Modified Calculation: The modified calculation method was developed by multiplying the DSM design strength of unperforated members by a strength reduction factor for perforated members. This reduction factor accounts for the influence of perforations on the overall buckling, local buckling, and distortional buckling stability of the member. The calculation process is simple and intuitive, offering high precision. Thus, this method may be considered as a promising choice for evaluating the high strength steel thin-walled perforated channel section axial compression members.

Table 18
Comparison of FE failure loads with different strength grade for C2-section specimens (t = 1.0 mm).

Specimen ID	P^{G500}_{FEA}	P^{Q235}_{FEA}	$P^{CP980}_{FEA}/P^{H500}_{FEA}$	$P^{CP980}_{FEA}/P^{Q235}_{FEA}$
C2L300	85.7	63.7	1.29	1.73
C2L300-W1	61.2	38.6	1.28	2.03
C2L300-F1W1	48.9	29.9	1.36	2.22
C2L900	77.6	57.5	1.02	1.38
C2L900-W1	49.2	32.3	1.33	2.02
C2L900-W2	45.6	27.2	1.24	2.08
C2L900-W3	45.2	27.4	1.30	2.15
C2L900-F1W1	38.6	24.3	1.33	2.12
C2L1500	61.3	54.3	1.07	1.21
C2L1500-W1	41.3	29.5	1.22	1.71
C2L1500-W2	39.7	27.5	1.18	1.70
C2L1500-W3	38.4	27.1	1.19	1.68
C2L1500-W5	37.2	26.4	1.25	1.76
C2L1500-F1W1	36.5	25.0	1.26	1.84
C2L1500-F2W2	34.0	24.0	1.23	1.75
C2L2000	42.0	39.9	1.00	1.06
C2L2000-W1	33.5	26.0	1.11	1.43
C2L2000-W2	31.7	25.1	1.11	1.40
C2L2000-W3	30.6	23.7	1.11	1.43
C2L2000-W5	30.1	24.0	1.10	1.38
C2L2000-F1W1	31.1	22.7	1.15	1.57
C2L2000-F2W2	29.0	21.5	1.14	1.54
P_m			1.19	1.69

Table 19
Comparison of FE failure loads with codified compression resistance predictions for C1-section specimens with no perforations.

Plate thickness (mm)	Specimen ID	P_{FEA}/P_{DSM}	P_{FEA}/P^{M}_{DSM}
0.6	C1L300	1.00	0.99
	C1L900	1.04	1.02
	C1L1500	1.14	1.12
	C1L2000	1.25	1.21
1.0	C1L300	1.08	1.05
	C1L900	0.97	0.94
	C1L1500	1.27	1.22
	C1L2000	1.23	1.18
2.0	C1L300	1.02	1.02
	C1L900	0.96	0.91
	C1L1500	1.04	0.99
	C1L2000	1.07	1.07
P_m		1.09	1.06
COV		0.099	0.096

Table 20
Comparison of FE failure loads with codified compression resistance predictions for C2-section specimens with no perforations.

Plate thickness (mm)	Specimen ID	P_{FEA}/P_{DSM}	P_{FEA}/P^{M}_{DSM}
0.6	C2L300	1.17	1.19
	C2L900	1.00	1.17
	C2L1500	0.80	0.94
	C2L2000	0.87	0.96
1.0	C2L300	1.06	1.07
	C2L900	0.73	0.86
	C2L1500	0.75	0.94
	C2L2000	0.91	0.97
2.0	C2L300	1.01	1.03
	C2L900	0.95	1.15
	C2L1500	0.94	0.98
	C2L2000	1.02	1.02
P_m		0.93	1.02
COV		0.139	0.100

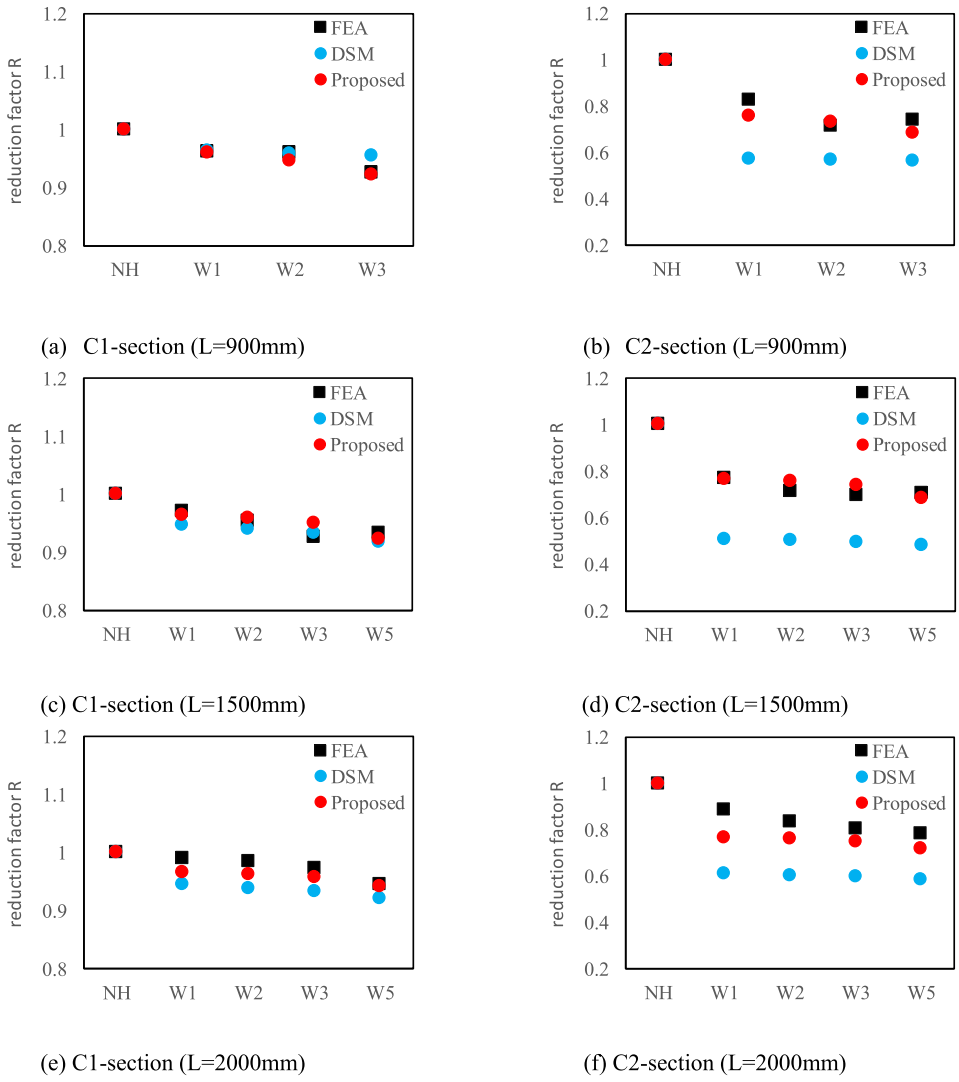

Fig. 22. Degradation of load versus web hole number.

CRediT authorship contribution statement

Jia-Hui Zhang: Conceptualization, Funding acquisition, Investigation, Methodology, Project administration, Supervision, Writing – original draft. **Jiaxin Wang:** Data curation, Formal analysis, Investigation, Software, Writing – original draft. **Shuluan Xu:** Data curation, Formal analysis, Investigation, Software. **Fangying Wang:** Investigation, Supervision, Validation, Writing – review & editing.

Declaration of Competing Interest

The authors declare that they have no known competing financial interests or personal relationships that could have appeared to influence the work reported in this paper.

Data availability

Data will be made available on request.

References

[1] C.D. Moen, B.W. Schafer, Experiments on cold-formed steel columns with holes, Thin-Walled Struct. 46 (2008) 1164–1182.
[2] C.D. Moen, B.W. Schafer, Elastic buckling of cold-formed steel columns and beams with holes, Eng. Struct. 31 (2009) 2812–2824.
[3] C.D. Moen, B.W. Schafer, Direct strength method for Design of Cold-Formed Steel Columns with holes, J. Struct. Eng. 137 (2011) 559–570.
[4] F.H. Smith, C.D. Moen, Finite strip elastic buckling solutions for thin-walled metal columns with perforation patterns, Thin-Walled Struct. 79 (2014) 187–201.
[5] AISI S100-16, North American Specification for the Design of Cold-Formed Steel Structural Members, American Iron and Steel Institute, 2016.
[6] M.P. Kulatunga, M. Macdonald, Investigation of cold-formed steel structural members with perforations of different arrangements subjected to compression loading, Thin-Walled Struct. 67 (2013) 78–87.
[7] M.P. Kulatunga, M. Macdonald, J. Rhodes, D.K. Harrison, Load capacity of cold-formed column members of lipped channel cross-section with perforations subjected to compression loading – part I: FE simulation and test results, Thin-Walled Struct. 80 (2014) 1–12.
[8] J. Zhao, J. Liu, C. Yu, W. Zhang, Test investigation and direct strength method on cold-formed steel compression members with web holes of different widths, Eng. Struct. 272 (2022) 114979.
[9] J. Zhao, J. He, B. Chen, W. Zhang, S. Yu, Test and direct strength method on slotted perforated cold-formed steel channels subjected to eccentric compression, Eng. Struct. 285 (2023) 116082.
[10] J. Zhao, S. Liu, B. Chen, Axial strength of slotted perforated cold-formed steel channels under pinned-pinned boundary conditions, J. Constr. Steel Res. 200 (2023) 107673.
[11] B. Chen, K. Roy, A. Uzzaman, G.M. Raftery, D. Nash, G.C. Clifton, P. Pouladi, J.B. P. Lim, Effects of edge-stiffened web openings on the behaviour of cold-formed steel channel sections under compression, Thin-Walled Struct. 144 (2019) 106307.
[12] B. Chen, K. Roy, A. Uzzaman, G.M. Raftery, J.B.P. Lim, Parametric study and simplified design equations for cold-formed steel channels with edge-stiffened holes under axial compression, J. Constr. Steel Res. 172 (2020) 106161.
[13] Z. Yao, K.J.R. Rasmussen, Perforated cold-formed steel members in compression. I: parametric studies, J. Struct. Eng. 143 (2017) 04016226.

[14] Z. Yao, K.J.R. Rasmussen, Perforated cold-formed steel members in compression. II: design, J. Struct. Eng. 143 (2017) 04016227.
[15] P. Zhang, M.S. Alam, Elastic buckling behaviour of Σ-shaped rack columns under uniaxial compression, Eng. Struct. 212 (2020) 110469.
[16] P. Zhang, M.S. Alam, Compression tests of thin-walled cold-formed steel columns with Σ -shaped sections and patterned perforations distributed along the length, Thin-Walled Struct. 174 (2022) 109082.
[17] X. Yan, Y. Xia, H.B. Blum, T. Gernay, Elevated temperature material properties of advanced high strength steel alloys, J. Constr. Steel Res. 174 (2020) 106299.
[18] X. Yan, Y. Xia, H.B. Blum, T. Gernay, Post-fire mechanical properties of advanced high-strength cold-formed steel alloys, Thin-Walled Struct. 159 (2021) 107293.
[19] Y. Xia, X. Yan, T. Gernay, H.B. Blum, Elevated temperature and post-fire stress-strain modeling of advanced high-strength cold-formed steel alloys, J. Constr. Steel Res. 190 (2022) 107116.
[20] N. Baddoo, A. Chen, High Strength Steel Design and Execution Guide, Steel Construction Institute, 2020.
[21] GB/T 228.1-2021, Metallic Materials-Tensile Testing-Part 1: Method of Test at Room Temperature, Standards Press of China, 2021 (in Chinese).
[22] F. Wang, O. Zhao, B. Young, Testing and numerical modelling of S960 ultra-high strength steel angle and channel section stub columns, Eng. Struct. 204 (2020) 109902.
[23] F. Wang, O. Zhao, B. Young, Flexural behaviour and strengths of press-braked S960 ultra-high strength steel channel section beams, Eng. Struct. 200 (2019) 109735.
[24] V.M. Zeinoddini, B.W. Schafer, Simulation of geometric imperfections in cold-formed steel members using spectral representation approach, Thin-Walled Struct. 60 (2012) 105–117.
[25] AISI S100-16, Commentary on North American Specification for the Design of Cold-Formed Steel Structural Members, American Iron and Steel Institute, 2016.